FISEVIER

Contents lists available at ScienceDirect

# Results in Engineering

journal homepage: www.sciencedirect.com/journal/results-in-engineering



# Research paper



# Effective properties of masonry structures and macro-model analysis with experimental verification

Hernán García a,c,\*, Juan Jiménez-Pacheco b,1, Jacinto Ulloa d,1

- <sup>a</sup> Facultad de Arquitectura, University of Cuenca, Av. 12 de Abril, Cuenca, 010203, Azuay, Ecuador
- <sup>b</sup> Red Sísmica del Austro, Civil Engineering Department, University of Cuenca, Av. 12 de Abril, Cuenca, 010203, Azuay, Ecuador
- Civil Engineering Department, University of Azuay, Av. 24 de Mayo 7-77, Cuenca, 010204, Azuay, Ecuador
- d Division of Engineering and Applied Science, California Institute of Technology, 1200 E. California Blvd., Pasadena, 91125, CA, USA

#### ARTICLE INFO

#### ABSTRACT

Keywords: Masonry Micro-model Macro-model Damage Masonry structures are the most prevalent type of buildings worldwide, and a significant portion are situated in seismic-prone areas. Thus, detailed information regarding their seismic strength and vulnerability is needed. The complexity of studying masonry structures lies in defining accurate and efficient models for representing masonry walls. In this context, there is a need for simplified methods that allow the modeling of masonry walls within a 3D structure. This work presents a methodology to define effective masonry properties from numerical analyses on representative volumes, using a damage model informed by experimental tests on units and mortar. These effective material properties serve as input parameters to model masonry walls within a macro-model approach, aiming to accurately capture the in-plane behavior and damage mechanisms with limited computational cost. The methodology is verified with experimental results and applied to real case studies in Cuenca, Ecuador.

#### 1. Introduction

Masonry buildings, the most common structures worldwide, are particularly vulnerable to earthquakes. However, research on masonry remains limited, for instance, when compared to reinforced concrete or steel structures. Further research is thus needed to refine current analysis methods and ensure accurate predictions of the global structural response and the behavior of the structural components. However, modeling masonry is challenging due to its heterogeneous nature and inherent non-linear behavior.

Several seismic assessment methods for masonry rely on idealized procedures [1,24,34,36] to capture the global response. These methods commonly model walls using 1D beam elements. Most idealized methods face difficulties in characterizing the connection between walls and other structural components, such as reinforced concrete columns and beams. In addition, the multiple damage mechanisms of masonry walls are not easily captured [8]. On the other hand, more dedicated models consider most interactions between masonry constituents using a full discretization of units, mortar, and interfaces [12,15,49]. Applying these modeling approaches to large walls or buildings implies high computational costs [25,28], particularly in 3D, and may be cumbersome to

implement. Hence, macro-modeling—an intermediate solution—arises as a valuable option [51].

Macro-models have been used for the seismic assessment of large and complex structures [27,35]. By treating masonry as a homogeneous continuum, this approach implies significant computational savings and an easier mesh generation process. While isotropic models are often used due to their simplicity and fewer material properties, it has been wellrecognized that masonry is better represented as an orthotropic medium. Hence, suitable non-linear constitutive models are required, which must accurately capture the orthotropic elasticity, strength, and softening response of the composite material. Elastoplasticity and damage models are typically employed for this purpose. Early references that address the yielding and maximum strength of different anisotropic materials include Hill [19,20], Hoffman [21], Tsai-Wu [67], and Dutko et al. [14]. Moreover, this problem may be addressed conveniently using tensor transformations, e.g., linear transformations of stress components and the concept of mapped stress tensor [6,7]. This approach describes the anisotropic behavior of a material through equivalent isotropic properties. In this context, a transformation tensor was defined by Oller et al. [45,46] to relate the stresses and strains in an orthotropic space to those

<sup>\*</sup> Corresponding author at: Facultad de Arquitectura, University of Cuenca, Av. 12 de Abril, Cuenca, 010203, Azuay, Ecuador.

E-mail addresses: hernan.garcia@ucuenca.edu.ec (H. García), juan.jimenez@ucuenca.edu.ec (J. Jiménez-Pacheco), julloa@caltech.edu (J. Ulloa).

Contributing authors.

in a mapped space, where an isotropic yield criterion is employed. While these mapping tensor methods focus on plasticity problems, the work of Pelà et al. [50,51] further considered continuum damage mechanics.

The success of macro-modeling approaches relies heavily on access to accurate and representative material properties. For masonry, such properties may be obtained from experimental testing [5]. Conducting tests on 1:1 scale walls or buildings in small laboratories is often impractical due to the high costs and lack of adequate equipment. Hence, tests on (properly defined) representative volumes are essential. In this context, numerical homogenization offers a viable alternative, providing averaged effective material properties from direct numerical simulations [26].

The effective stress-strain relations of macro-models based on homogenized material properties require the elastic stiffness constants and the generally non-linear tangent operator. In this context, Lourenço [25] showed accurate results for an elastoplastic model considering representative volumes of layered structures. For masonry, a non-layered composite, the author employed a two-step homogenization along the two main material axes. In this case, results [25] showed that without discretizing the geometry of the components, the method accurately predicts the elastic response. However, it can yield significant errors in the non-linear stage. Luciano and Sacco [33] further proposed a damage model based on periodic homogenization. The method identifies eight damaged/undamaged states based on different mortar crack patterns and allows the study of damage evolution in masonry, considering simplified geometries.

The non-linear homogenization of masonry presents considerable complexity, particularly during softening, due to mathematical challenges, difficulties in predicting collapse displacements, limitations in defining micromechanical damage, and representing frictional behavior. While improved methodologies are still under development [22, 26,41], Petracca [54] proposed a different approach, employing a fracture energy-based regularization for two-scale computational homogenization. This procedure allows first-order homogenization for quasibrittle materials, considering the characteristic finite element size at both micro- and macro-scales and the size of the representative volume element (RVE). However, solving a micro-scale boundary volume problem at every macroscopic time step/iteration implies a computational burden. Computational multi-scale methods, of course, share this issue in general. In the present study, this approach is taken as the point of departure; however, rather than performing two-scale computations, we aim to identify the averaged properties of a macro-scale damage model.

A numerical model suitable for deriving effective properties must describe the different stages of masonry behavior. For this purpose, it is possible to use detailed, 2D or 3D, micro-modeling of single-wythe walls. The 2D case is efficient and can provide accurate results [18,58] for walls with brick assemblies that follow a regular pattern [2,53]. A computationally efficient option in this context is limit analysis [3,59], which determines the ultimate load-carrying capacity and failure mode. However, this approach does not capture the softening response. Another option is to use discrete models [3,37,59] with zero-thickness interface elements characterized by cohesive-frictional constitutive laws [18]. The brick units are commonly described as rigid blocks and the non-linear behavior is limited to the interfaces [13]. This approach allows for material characterization under different loading conditions [53,58] but is not suitable if the non-linear behavior of the bricks plays an important role, e.g., when the failure probability is higher for units than for mortar [38]. Indeed, in masonry walls with low-strength bricks under high compressive-shear states, damage can appear in the units before the mortar, modulating the global response. A viable alternative uses continuum elements for the bricks and the mortar, with both materials exhibiting non-linear behavior. Nevertheless, standard FEMcontinuum methods present well-established difficulties in capturing softening and failure mechanisms [15] and, when at all possible, require fine discretizations to yield accurate results [28].

The continuum damage approach for masonry structures proposed by Petracca et al. [58] overcomes most of these limitations, building upon previous damage models by Cervera et al. [10], Faria et al. [16], and Wu et al. [71]. It employs an anisotropic damage model [50] with different degradation mechanisms for loading/unloading in tension and compression. The model is deemed more efficient than plasticity approaches, allowing a straightforward description of damage in units and mortar using two scalar-valued internal variables. These variables are evaluated explicitly, without local iterative schemes. Moreover, the model includes an implicit control of dilatancy in the mortar joints, without resorting to plastic potentials. The authors present an implicit/explicit integration scheme [44] that improves convergence, avoiding numerical instability in the softening stage, where a fracture energy-based approach provides regularization.

The present paper aims to identify effective properties for different types of masonry, including walls with low-strength units, for use in a macro-modeling approach. To describe the non-linear response of the constituent materials, we resort to the continuum damage model of Petracca et al. [58], informed by experimental tests on brick units and mortar. We explore a simple methodology to derive effective masonry properties from numerical simulations on RVEs. The obtained properties are then used as input parameters of a macro-scale continuum model, avoiding the computational burden of two-scale analysis. The methodology applies to masonry walls with any regular arrangement (single-wythe or double-wythe masonry walls). The validation is twofold, considering (i) macro-model simulations with experimental verification for the shear walls tested by Raijmakers and Vermeltfoort [61], and (ii) size effects and mesh sensitivity, essential for materials with softening. Moreover, the methodology is applied to obtain the effective properties of two typical masonry walls used in buildings in Cuenca, Ecuador, considering uncertainty in the materials and providing a representative database for construction in the region.

#### 2. Micro-modeling approach

We resort to continuum damage mechanics to describe the behavior of composite masonry structures [54,58]. The parameters of the damage model are established from experimental tests on bricks and mortar. This section is the basis for the micro-modeling approach, used to derive effective macroscopic properties from representative volumes in the subsequent sections.

#### 2.1. Damage model

We consider a tension/compression damage model [58] that has shown to be robust and accurate for both the micro- and macro-modeling of masonry structures [56]. It represents an enhancement of previous models [10,16,71], providing a convenient control of dilatancy under shear stress states. The resulting micro-model is simple and efficient, and avoids nested iterative procedures by explicitly updating two scalar-valued damage internal variables. The formulation is briefly summarized below for the readers' convenience.

The stress tensor of the constitutive model is defined in terms of two damage parameters, one for the positive part and one for the negative part:

$$\sigma = (1 - d^{+})\bar{\sigma}^{+} + (1 - d^{-})\bar{\sigma}^{-} \tag{1}$$

where  $d^+$  and  $d^-$  are the two damage scalars that measure the amount of damaged material from 0 (no damage) to 1 (complete damage). Moreover,  $\bar{\sigma}^+$  and  $\bar{\sigma}^-$  are, respectively, the positive and negative parts of the effective stress tensor  $\bar{\sigma}$ , representing the stress on the effective resistant section.  $\bar{\sigma}$  is calculated from the linear elastic relation

$$\bar{\sigma} = \mathbb{C} : \epsilon \tag{2}$$

where  $\mathbb C$  is the fourth-order isotropic stiffness tensor and  $\epsilon$  is the strain tensor. The positive and negative parts of the effective stress tensor are given by

$$\bar{\sigma}^{+} = \sum_{i=1}^{3} \langle \bar{\sigma}_{i} \rangle \, p_{i} \otimes p_{i} \tag{3}$$

$$\bar{\sigma}^- = \bar{\sigma} - \bar{\sigma}^+ \tag{4}$$

where  $\bar{\sigma}_i$  is the ith principal stress,  $p_i$  is the unit vector of the associated principal direction, and  $\langle \cdot \rangle$  are the Macaulay brackets, returning zero for negative values and the enclosed expression for positive values. Thus, the positive part of the effective stress tensor  $\bar{\sigma}^+$  represents the recomposition of the positive eigenvalues multiplied by the outer product of the associated eigenvectors.

The model includes failure criteria for tension and compression. In the 2D case, the tensile failure surface is given in terms of an equivalent stress measure  $\tau^+$ :

$$\tau^{+} = H(-\bar{\sigma}_{\min}) \left[ \frac{1}{1 - \alpha} \left( \alpha \, \bar{I}_{1} + \sqrt{3 \, \bar{J}_{2}} + \beta \, \langle \, \bar{\sigma}_{\max} \rangle \right) \frac{f_{t}}{f_{c}} \right] \tag{5}$$

with

$$\alpha = \frac{k_{b} - 1}{2k_{b} - 1}, \qquad \beta = \frac{f_{c}}{f_{t}} (1 - \alpha) - (1 + \alpha)$$
 (6)

Here,  $\bar{I}_1$  is the first invariant of the effective stress tensor,  $\bar{J}_2$  is the second invariant of the effective deviatoric stress tensor,  $\bar{\sigma}_{\max}$  is the maximum effective principal stress,  $k_{\rm b}$  is the ratio of bi-axial to uniaxial compressive strengths,  $f_{\rm c}$  is the maximum compressive stress, and  $f_{\rm t}$  is the tensile strength. On the other hand, the compression failure surface is defined as

$$\tau^{-} = H(-\bar{\sigma}_{\min}) \left[ \frac{1}{1 - \alpha} \left( \alpha \, \bar{I}_1 + \sqrt{3 \, \bar{J}_2} + k_1 \, \beta \, \langle \, \bar{\sigma}_{\max} \rangle \right) \right] \tag{7}$$

Here, the scalar  $k_1$  takes values between 0 (Drucker-Prager criterion) and 1 (Lubliner et al. criterion [32]). This parameter implicitly controls dilatancy (volume change due to shear stress) by defining the size of the compressive surface in the tension/compression quadrants. A larger compressive surface (relative to the tensile surface) results in higher dilatancy.

In equations (5) and (7), the Heaviside function

$$H(x) = \begin{cases} 0 & x < 0 \\ 1 & x > 0 \end{cases}$$
 (8)

is introduced to allow the tensile surface to evolve when at least one principal stress is positive and the compressive surface to evolve when at least one principal stress is negative [58], hindering unrealistic damage mechanisms from being active under arbitrary stress states.

The model takes into account irreversible damage. This condition is characterized by two damage thresholds,  $r^+$  and  $r^-$ , representing the largest positive and negative damage values reached by  $\tau^\pm$  at any time step t in the loading history:

$$r^{\pm} = \max\left(r_0^{\pm}, \max_{0 \le n \le i} \tau^{\pm}\right) \tag{9}$$

where  $r_0^{\pm}$  represents the initial limits in tension ( $f_{\rm t}$ ) and compression ( $f_{\rm c0}$ ). In this way, the damage criteria read

$$\tau^{\pm} - r^{\pm} = \le 0 \tag{10}$$

The evolution law for tensile damage has the explicit form [58]

$$d^{+}(r^{+}) = 1 - \frac{r_{0}^{+}}{r^{+}} \exp \left\{ 2H_{\text{dis}} \left( \frac{r_{0}^{+} - r^{+}}{r_{0}^{+}} \right) \right\}$$
 (11)

where  $H_{\rm dis}$  is a softening parameter adjusted according to the dissipative zone size  $l_{\rm dis}$  [4,43], taken equal to the finite element discretization

length,  $l_{\rm dis} \equiv l_{\rm ch}$ , in order to achieve mesh-insensitive results. In particular:

$$H_{\rm dis} = \frac{l_{\rm dis}}{l_{\rm mat} - l_{\rm dis}}, \qquad l_{\rm mat} = \frac{2 E G_{\rm f}}{f_{\star}^2}$$
 (12)

where  $G_{\rm f}$  is the fracture energy in tension, obtained from the uniaxial stress-strain curve, while

$$g_{\rm f} = \left(1 + \frac{1}{H_{\rm dis}}\right) \frac{f_{\rm t}^2}{2E} \tag{13}$$

is the specific fracture energy per unit volume. In this way, the following condition is satisfied:

$$g_{\rm f} l_{\rm dis} = G_{\rm f} \tag{14}$$

This model produces a typical uniaxial response [29], characterized by the initial elastic stiffness up to the peak strength and exponential softening thereafter.

On the other hand, for the evolution of the compressive damage index  $d^-$ , Petracca et al. [58] proposed an ad hoc expression based on a composite curve using a uniaxial hardening/softening law. Three quadratic Bézier curves, each controlled by three control points, characterize the linear  $(\epsilon_0, \sigma_0)$ , hardening, peak  $(\epsilon_p, \sigma_p)$  and softening parts of a uniaxial compressive test. The softening part is represented by a residual  $(\epsilon_r, \sigma_r)$  and ultimate state  $(\epsilon_u, \sigma_u)$ . The damage index  $d^-$  as a function of the damage threshold  $r^-$  is updated using

$$d^{-}(r^{-}) = 1 - \frac{\sum(\xi)}{r^{-}} \tag{15}$$

where  $\sum(\xi)$  represents a stress state in the Bézier curves as a function of  $\xi = r^-/E$ .

Note that equation (14), relating the specific fracture energy with the characteristic finite element size, is well-established from the work of Bažant et al. [4] and has been adopted in several contributions [9,43,54] to achieve mesh-insensitive results in finite element simulations during softening. This feature is crucial for the present numerical studies.

#### 2.2. Material properties

The damage model introduced in section 2.1 requires the following properties: compressive strength  $f_{\rm c}$  and corresponding strain  $\epsilon_{\rm p}$ , Young's modulus E, Poisson's ratio v, tensile strength  $f_{\rm t}$ , compressive elastic strength  $f_{\rm c0}$ , compressive residual strength  $f_{\rm r}$ , fracture energies ( $G_{\rm t}$  for tension and  $G_{\rm c}$  for compression), compressive biaxial strength factor  $k_{\rm b}$ , and shear-compression reduction factor  $k_{\rm l}$ . Here, these properties are obtained from experimental tests on bricks and mortar cubes. In this process, it is relatively simple to obtain the compressive strength  $f_{\rm c}$  and the corresponding strain  $\epsilon_{\rm p}$  from compressive tests, without complex equipment. These two parameters are the basis for estimating additional properties.

The remaining material parameters are derived as follows. Firstly, the expression proposed by Yassin [72] is employed to estimate Young's modulus of bricks and mortar as

$$E = \frac{2f_{\rm c}}{\epsilon_{\rm p}} \tag{16}$$

The Poisson's ratio, after consulting the work of several authors [42,47, 48,69], is chosen 0.18 for hollow bricks, 0.17 for solid bricks, and 0.20 for mortar. The tensile strength of bricks and mortar is a function of their corresponding compressive strength. The value is sampled from a log-normal distribution with an average of 0.07  $f_{\rm c}$  [63,64] and a standard deviation of 0.007  $f_{\rm c}$ . The units of  $f_{\rm c}$  must be N/mm². Compressive elastic strengths of brick  $f_{\rm c0b}$  and mortar  $f_{\rm c0m}$  and compressive residual strengths of brick  $f_{\rm rb}$  and mortar  $f_{\rm rm}$  are defined as 1/3 and 1/10 of their corresponding compressive strength. These values could be modified or adjusted from experimental tests.

Secondly, since small equipment cannot capture softening during compressive tests (the analysis stops after reaching the maximum strength), the fracture energies are defined as functions of strength. Lourenço and Milani [30], Lourenço and Rots [29], and Vasconcelos et al. [68] proposed to estimate fracture energies as the ratio between strength and energy (ductility index), suggesting  $G_{\rm c}=1.6\,f_{\rm c}$  and  $G_{\rm t}=0.029\,f_{\rm t}$ , the strength values in N/mm and the fracture energies in N/mm². Finally, the values of  $k_{\rm b}$  vary between 1 and 1.2 for bricks and mortar, and  $k_{\rm l}$  can be assumed as 0 for the units and 0.2 for mortar [25,57].

#### 3. Macro-modeling and experimental verification

This section presents the macro-modeling approach informed by effective properties. The overall methodology is as follows. First, the parameters of the micro-model are established from experimental tests on bricks and mortar (section 2.2). Then, RVEs of a masonry wall are defined and subjected to numerical analyses under different loading conditions. Then, results from the numerical calculations, namely the stress-strain and stress-displacement curves, are used to determine effective properties. As a crucial step, we consider orthotropic conditions, relying on the tensor mapping procedure of Pelà [52] and Pelà et al. [50]. To assess the accuracy of the macro-modeling approach, we take the experimental shear wall results of Raijmakers and Vermeltfoort [61] as a benchmark. Consequently, effective properties are extracted from RVEs representing the bonding pattern of walls J4D and J2G [61], analyzed under compressive, tensile, and shear forces.

## 3.1. Orthotropic damage model

Masonry is modeled at the macro-level as a homogeneous orthotropic continuum, considering the arrangement of its components and their interaction. The orthotropic behavior is simulated using a tensor mapping procedure that establishes a mathematical relationship between the anisotropic real space and an auxiliary mapped space, greatly simplifying the modeling process [51].

The non-linear behavior is again represented by the continuum damage model of subsection 2.1, where the damage parameters now evolve independently in different material axes for tension and compression. To this end, the real stresses are transformed into the mapped space using fourth-order transformation tensors that represent the anisotropic properties of the material. The damage variables and total stresses are computed in the mapped space and then returned to the real orthotropic stress space to update the internal forces. The algorithm is presented in Pelà et al. [51] for the analysis of masonry structures.

In orthotropic behavior, axial and shear strains in one direction are independent. Additionally, there is no coupling between shear stresses acting on different planes. Thus the resulting orthotropic relation between stresses and strains in plane stress conditions is

$$\begin{bmatrix} \sigma_{11} \\ \sigma_{22} \\ \sigma_{12} \end{bmatrix} = \begin{vmatrix} \frac{E_1}{1 - \nu_{12} \nu_{21}} & \frac{\nu_{21} E_1}{1 - \nu_{12} \nu_{21}} & 0 \\ \frac{\nu_{12} E_2}{1 - \nu_{12} \nu_{21}} & \frac{E_2}{1 - \nu_{12} \nu_{21}} & 0 \\ 0 & 0 & G_{12} \end{vmatrix} \begin{bmatrix} \epsilon_{11} \\ \epsilon_{22} \\ 2 \epsilon_{12} \end{bmatrix}$$
(17)

where  $E_1$  and  $E_2$  are the Young's modulus in the x-direction and y-direction, respectively,  $v_{12}$  and  $v_{21}$  are the two Poisson coefficients and  $G_{12}$  is the shear modulus in the 1-2 direction.

# 3.2. Effective properties

An RVE represents the smallest volume element that captures the essential characteristics of the microstructure and allows an objective prediction of effective properties. In the present work, we derive effective material properties from RVEs of single-wythe masonry walls using the numerical damage framework of section 2 as a micro-modeling approach. As discussed before, regularization is achieved during softening by taking the characteristic length equal to the finite element size.

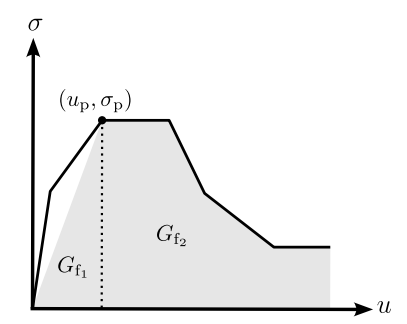
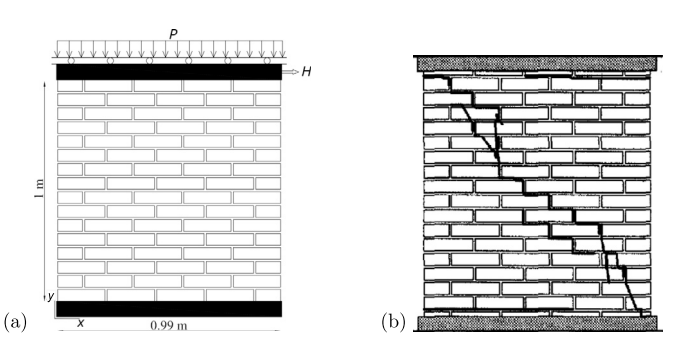


Fig. 1. Graphical illustration of the fracture energy per unit area (grey) from idealized stress-displacement curves.



**Fig. 2.** (a) Scheme of the experimental test setup of wall J4D consisting of 18 rows of bricks and mortar, two of which are attached to steel beams (black), and the loading conditions in two stages [70]. In the first stage, a uniform vertical force P is applied. In the second stage, a displacement-controlled lateral load H is applied. (b) Experimental crack patterns for wall JD4 after an incremental displacement of 4 mm, adapted from Lourenço [25].

Analyses in two directions are necessary to define the effective properties of the orthotropic medium. Thus, the numerical simulations are conducted in directions perpendicular to the bed joints (y or 2) and perpendicular to the head joints (x or 1). The results are the basis for deriving the effective properties, employing the average stresses, average strains, and total displacements of the RVEs under different loading conditions. At each load increment, the stress  $\sigma$  is computed by averaging the resulting forces and dividing by the acting area of the RVE. The corresponding strain  $\epsilon$  is determined by averaging the displacement at each increment and dividing by the initial length of the specimen in the loading direction. A typical response curve consists of four characteristic stages: elasticity, yielding, maximum strength, and softening.

For the elasticity parameters, compressive tests yield an estimate for Young's modulus, computed using Hooke's law in 1D as  $E=\sigma/\varepsilon$  during the elastic stage. Similarly, shear tests provide the shear modulus during the elastic stage as  $G=(VH)/(A\,\delta)$ , where V is the total shear force, H is the RVE height, A is the RVE area, and  $\delta$  is the average lateral displacement. On the other hand, the compression and tensile strengths follow from the corresponding maxima of each curve. For compression, the elastic compressive strength is assumed to be 1/5 of the peak strength, approximately corresponding to the value where the uniaxial curve becomes inelastic. The compressive residual strength is the stress (at a strain higher than  $\varepsilon_{\rm p}$ ) whose value decreases to less than or equal to 80% of the peak strength (it is assumed that the RVEs fail at this value).

Finally, the areas under the compressive and tensile *force-displacement* curves estimate the compressive and tensile fracture energies [25,29], respectively. This approach will be crucial for counteracting the expected size effect, as shown numerically in section 4.5. Fig. 1 illustrates the areas under the curve that represent fracture energy in units of energy per unit length. The limit on the right side of  $G_{\rm f_2}$  represents the ultimate compressive strength.

Table 1
Material properties of bricks and mortar adapted from Lourenço [25, 58].

Property	Values Brick	Mortar	Units
	Brick	Mortar	
Young's modulus $E$	16700	850	[MPa]
Poisson's ratio $\nu$	0.15	0.15	[-]
Tensile strength $f_t$	2.0	0.25	[MPa]
Tensile fracture energy $G_{\rm t}$	0.08	0.018	[N/mm]
Compressive elastic strength $f_{c0}$	8.0	3.0	[MPa]
Compressive strength $f_c$	12.0	10	[MPa]
Compressive residual strength $f_r$	1.0	2.0	[MPa]
Compressive fracture energy $G_c$	6.0	80.0	[N/mm]
Strain at peak strength $\epsilon_{\rm p}$	0.004	0.04	[-]
Compressive biaxial strength factor $k_b$	1.2	1.2	[-]
Shear-compression reduction factor $k_1$	0.0	0.16	[-]

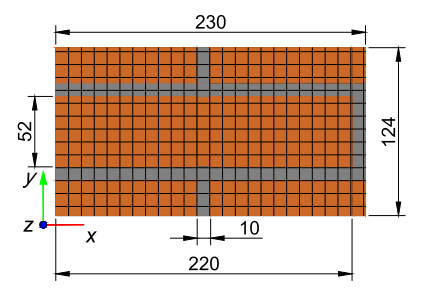


**Fig. 3.** RVE representing the pattern of wall JD4, showing the mesh (black borders) representing bricks (brown fills) and mortar (gray fills).

# 3.3. Wall J4D

Let us now present a validation of the macro-modeling approach for characterizing masonry walls. We consider, as a benchmark, wall J4D of the TU Eindhoven shear walls tested by Raijmakers and Vermeltfoort [61] in 1992, as part of the CUR [62] project. The dimensions of the wall (Fig. 2) are 0.99 m long, 1 m high, and 0.098 m wide, consisting of 18 courses of wire-cut solid bricks and mortar. The upper and lower courses are fixed in steel sections. The bricks are 0.204 m long, 0.0525 m high, and 0.098 m thick. The mortar is 0.01 m thick and composed of cement, lime, and sand in a volume ratio 1:2:9.

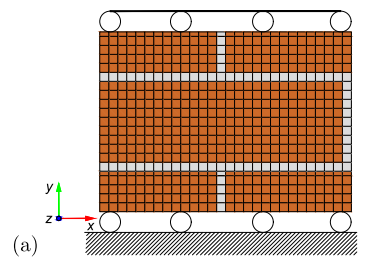
During the experiment, two actuators hold the upper steel beam horizontally (Fig. 2) while the lower beam is fixed. A compressive pressure of  $0.3~\mathrm{N/mm^2}$ , resulting in a total load of 30 kN, is applied to the upper beam. In the second loading stage, lateral displacements are applied incrementally until failure. Fig. 2b presents the crack pattern in the final state. Diagonal cracks form around the mortar interface, typical of shear failure. The three lower-right bricks show diagonal cracks, while the lower-left section shows detachment of brick-mortar interfaces.

The following subsections aim to reproduce the experimental observations using the simplified framework proposed in the present study. The accuracy of the orthotropic macro-model solution in approximating the experimental results will represent the first validation of this approach.

# 3.3.1. RVE analyses and effective properties

The framework discussed in section 3.2 for computing effective masonry properties is now applied to an RVE considering the wall's bonding pattern (Fig. 3). Table 1 summarizes the material properties of units and mortar, obtained as discussed in subsection 2.2, based on the compressive strengths from Lourenço [25].

The numerical analyses consider compressive, tensile, and shear loading under plane stress conditions. Fig. 4 illustrates the boundary conditions. The bottom nodes are fixed in both directions for the compressive and tensile analyses, while an equal-degree-of-freedom constraint is assigned to the top nodes. A distributed vertical load is first



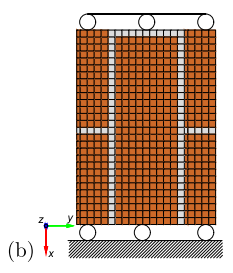


**Fig. 4.** Scheme of boundary conditions for (a) RVE perpendicular to bed joint (*y* or 2 direction) and (b) RVE perpendicular to the head joint (*x* or 1 direction).

**Table 2**Effective masonry properties for wall J4D obtained from compressive, tensile, and shear analyses in two directions.

Property	Values		Units
	2-direction	1-direction	
Young's modulus $ar{E}$	4142.7	9395.4	[MPa]
Shear modulus $\bar{G}$	1521.4	1521.4	[MPa]
Poisson's ratio $\bar{\nu}$	0.20	0.17	[-]
Tensile strength $\bar{f}_{_{\mathrm{f}}}$	0.21	0.56	[MPa]
Tensile fracture energy $ar{G}_{_{\mathrm{f}}}$	0.02	0.05	[N/mm]
Compressive elastic strength $\bar{f}_{c0}$	3.6	3.1	[MPa]
Compressive strength $\bar{f_{\rm c}}$	10.7	9.4	[MPa]
Compressive residual strength $\bar{f}_{r}$	1.8	2.5	[MPa]
Compressive fracture energy $\bar{G}_{c}$	6.8	16.2	[N/mm]
Strain at peak strength $\bar{e}_{p}$	0.008	0.004	[-]
Compressive biaxial strength factor $\bar{k}_b$	1.2	1.2	[-]
Shear-compression reduction factor $\bar{k}_1$	0.0	0.0	[-]

applied until reaching a target displacement. The initial loads are -1 N/mm for compression and 0.1 N/mm for tension. Then, displacement-controlled increments in 200 steps are applied, leading to maximum reaction forces (compressive or tensile strength) followed by softening behavior. The target displacement for compression and tension is 5.0 mm and 0.25 mm, respectively. The top boundary conditions for the shear simulations are different. A prescribed relative displacement constrains the top nodes while forcing them to reach a target displacement of 1 mm. These conditions keep the top nodes parallel to the bottom nodes. Vertical displacement of the top surface is allowed.

The analyses under plane stress conditions employ the penalty method to enforce constraints, while equilibrium is reached at each time step using the Krylov-Newton [65] iteration method. The tolerance criteria to check for convergence is 0.0001. The analysis takes approximately 30 s using a computer with an i7-8750 (2.20 GHz) processor and 16 GB of RAM.

Table 2 highlights the orthotropic properties derived from wall J4D RVEs in the y and x directions. As discussed in section 3.2, the average stress-strain curves from the compressive and tensile analyses (Fig. 5, a to d) provide the effective Young's modulus, elastic compressive strength, peak strength (compressive strength), residual strength, and tensile strength. On the other hand, the shear analyses (Figs. 5e and 5f) provide the shear modulus during the elastic stage. Finally, we obtain compressive and tensile fracture energies from the corresponding stress-displacement curves. As mentioned previously, this procedure provides a simple approach to alleviate the expected size effects in the softening response; this delicate point is addressed numerically in section 4.5 and not reproduced here for brevity.

#### 3.3.2. Macro-model analysis

Fig. 6 presents the numerical representation of wall J4D. The wall is discretized using quadrilateral elements under plane-stress conditions in OpenSees, using STKO [55]. The boundary conditions replicate the experimental test setup. The bottom nodes are fixed in the x and z directions. A distributed vertical load of 30 N/mm, simulating the 0.3 N/mm<sup>2</sup> of the experimental test, is assigned to the top elements of the

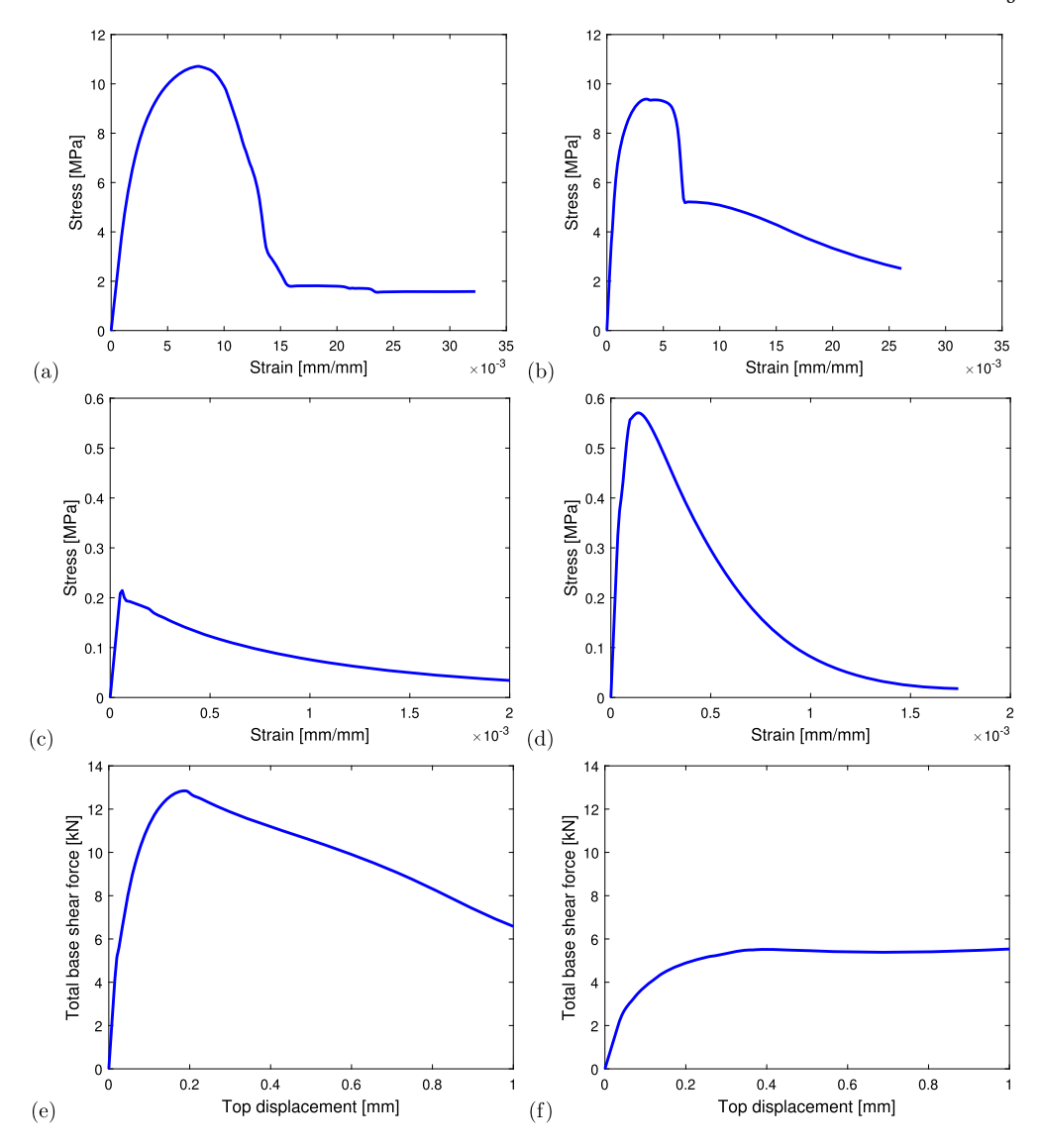


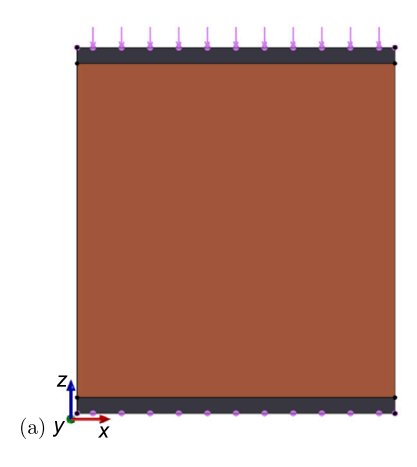
Fig. 5. Stress-strain curves resulting from compressive loading on RVEs (a) perpendicular to bed joints and (b) perpendicular to head joints, and from tensile forces on RVEs (c) perpendicular to bed joints and (d) perpendicular to head joints. Force-displacement curves from top lateral loading on RVEs (e) parallel to bed joints and (f) parallel to the head joints.

FEM model. This procedure is load-controlled and performed in 10 steps (it is assumed that the response will only be elastic). A second loading stage starts by imposing the vertical displacement on the top nodes corresponding to the last displacement state from the previous analysis. An equal-degree-of-freedom constraint is imposed on the upper nodes so that the elements representing the steel beam remain horizontal. Then, a prescribed lateral displacement of 4 mm is imposed on the top nodes in 200 steps. Equilibrium is reached at each time step using the Krylov-Newton iteration method [65].

Fig. 7 compares five curves: four numerical simulations and the experimental results. The numerical solutions include cases using the two sets of effective properties (in directions x and y) separately for isotropic macro-model analyses, a case using all the effective properties for orthotropic macro-model analysis, and the direct micro-model solution. The two isotropic solutions fail to approximate the wall's maximum strength and almost the entire experimental curve. The isotropic curve representing the wall's y-direction only matches the initial elastic stage of the experiment but overestimates the peak force. This effect is even more pronounced in the x-direction isotropic case. These re-

sults confirm that effective isotropic properties for masonry may not be representative. Conversely, the orthotropic homogenized solution shows excellent agreement with the experimental data, comparable to that of the micro-model solution in predicting the behavior of the wall in its elastic, inelastic, and softening stages.

Fig. 8 illustrates the horizontal displacement of the micro-model and orthotropic macro-model simulations after reaching a maximum top lateral displacement of 4 mm. Both solutions exhibit a clear path that identifies the separation of the wall into two parts. Additionally, both solutions display similar behavior corresponding to the experimental failure mode (Fig. 2b) and the response indicated in Fig. 7. Note that the top-left and bottom-right locations of fracture initiation are very close. However, the micro-model solution presents a slightly different trajectory. It primarily follows the path of the mortar bedding, which is not explicitly represented in the macro-model. Nevertheless, at a much lower computational cost, an overall reasonable agreement is observed, both in terms of the force-displacement response and the failure path.



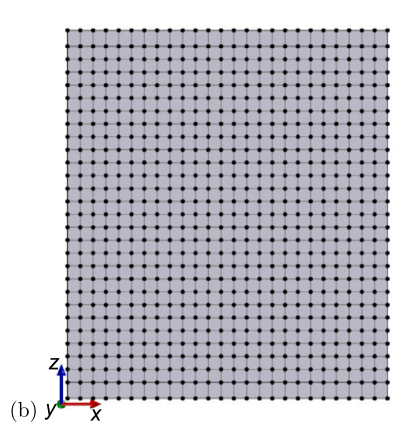
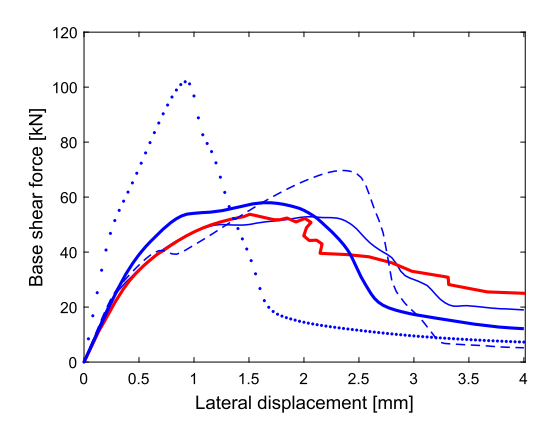


Fig. 6. (a) STKO representation of steel profiles (black), wall J4D masonry (brown), and boundary conditions (purple). (b) Finite element discretization using 856 elements and 754 nodes; the element size is 40 mm.



**Fig. 7.** Force-displacement curves from experimental results (red line), numerical micro-model analysis (blue line), macro-model orthotropic analysis (blue tick line), and macro-model isotropic analysis with materials properties on the *y*-direction (blue dashed line) and macro-model isotropic analysis with materials properties on the *x*-direction (blue dotted line).

# 3.4. Wall J2G

Fig. 9a presents the experimental setup of wall J2G [61], with an opening, while Fig. 9b shows the crack patterns. Most cracks form along the mortar joints, while only three bricks crack: one at the upper-left corner and two at the lower-right corner.

Fig. 10 illustrates a macro-model representation of wall J2G, with Fig. 10a depicting the model and Fig. 10b representing the corresponding finite element discretization. Table 2 presents the effective properties of wall J4D, which are also employed for wall J2G since the wall is made from the same materials. The boundary conditions are also the same. However, now the elements representing wall J2G are four-node parametric shell elements [31] instead of the quadrilateral elements used for wall J4D.

Fig. 11 shows the force-displacement curves, indicating changes in wall response, i.e., the onset of inelastic behavior, peak force, and ultimate displacement. The macro-model shows an accurate prediction of the elastic stage ( $u_{\rm x}=0.40$  mm) and the maximum strength. However, we observe a substantial stress decay (softening) after reaching the peak strength, which differs from the experimental result. This response is the case for both micro and macro-model predictions.

Figs. 12 and 13 depict tensile damage indices and maximum principal stresses at four displacement levels, as obtained from the macromodel FEM solution. Damage starts at the wall's lower-left and upperright corners. Fig. 13a shows tensile stress indicating possible detachments on the upper-right and bottom-left corners (Fig. 12a). Under

increasing lateral displacement, the damage areas increase (Fig. 12b), and the wall presents the highest compressive stresses (Fig. 13b). Then, the model shows severe damage at nearly 7 mm of lateral displacement (Fig. 12c). Splitting of the wall at a lateral displacement of 20 mm along the opening between the upper-left and bottom-right corners is evident due to extensive damage (Fig. 12d). The failure pattern of the wall is consistent with the experimental result depicted in Fig. 9.

Softening is triggered after reaching the maximum strength (Fig. 11) due to high tensile stresses (Fig. 13b) on the upper-left and bottom-right corners of the opening, resulting in possible longitudinal cracks. The final stage shows a pronounced softening response since most of the wall is under tensile stresses (Figs. 13c and 13d) that exceed the material's tensile strength. In this case, the micro-model and the macro-model numerical solutions depart considerably from the experimental post-peak response. In particular, the experimental force-displacement curve (Fig. 11) shows a ductile response with softening after reaching a lateral displacement of 13 mm. Wall J2G reaches a final displacement of 20 mm, more significant than the displacement of wall J4D under the same compressive loading. A possibility for the considerable difference after the post-peak response is that the model lacks the macroscopic plasticity that results from friction at the interfaces. This limitation is a worthwhile starting point for future research.

So far, we have shown numerically that the macro-damage model of Petracca et al. [58] informed by effective masonry properties from micro-model analyses provides an efficient alternative to direct numerical simulations, with a comparable ability to reproduce experimental observations. The following section will further delve into RVE analysis in a real case study, considering uncertainty in the material properties, size effects, and mesh sensitivity.

## 4. Application to Ecuadorian masonry

We apply the proposed methodology to estimate the effective properties of typical masonry systems of buildings in Cuenca, Ecuador. Similar to section 3, the procedure comprises four stages:

- Evaluating the material properties for bricks and mortar for the damage model of section 2, using experimental data from conventional materials in the region.
- 2. Defining RVEs for two typical masonry walls of buildings in Cuenca.
- Numerically testing the RVEs under compressive, tensile, and shear loading in two directions, considering uncertainty in the material properties for bricks and mortar.
- Estimating a database of effective properties from the numerical results.

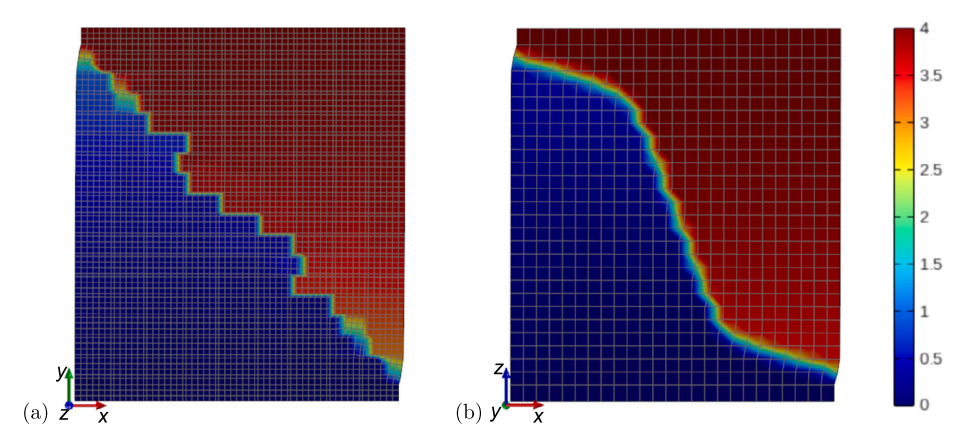
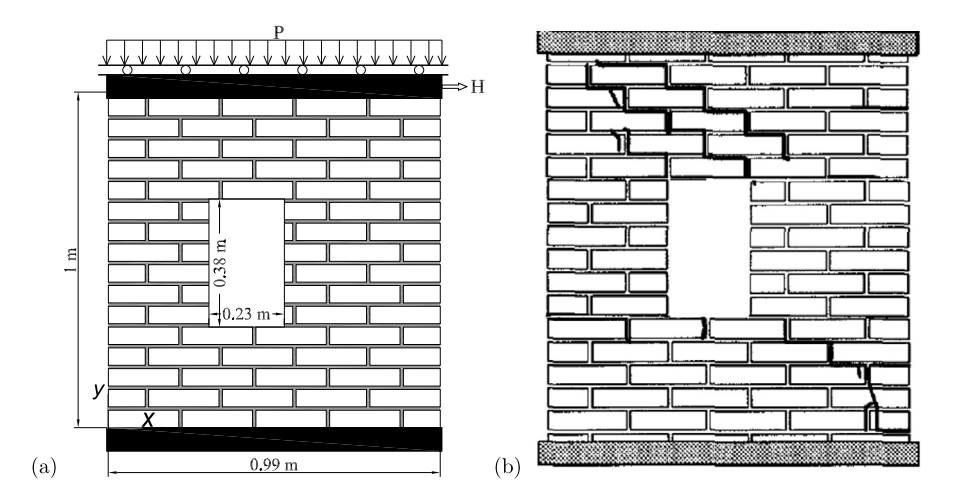


Fig. 8. Lateral displacement of wall J4D in mm (color bar) obtained using (a) the full micro-model and (b) the orthotropic macro-model. Superimposed on both figures are the mesh edges (gray lines). The displacements are scaled with a factor of 5.



**Fig. 9.** (a) Scheme of the experimental test setup of wall J2G, consisting of 18 rows of bricks and mortar, two of which are attached to steel beams (black), and the loading conditions in two stages [61]. In the first stage, a uniform vertical force *P* is applied. In the second stage, a displacement-controlled lateral load *H* is applied. (b) Experimental crack patterns for wall J2G. Adapted from Laurenço [25].

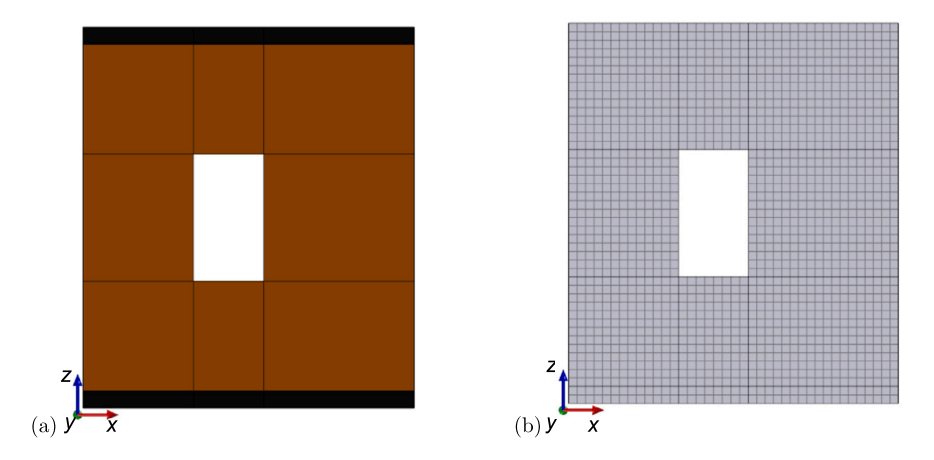
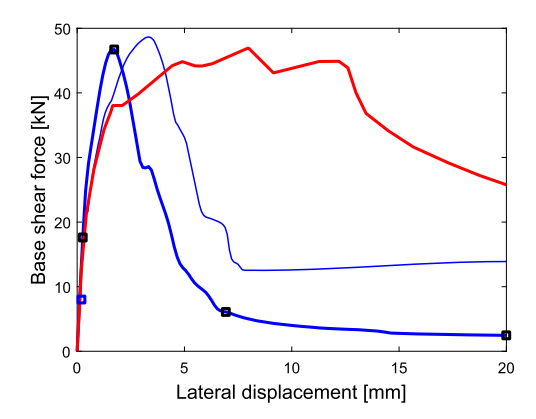


Fig. 10. (a) STKO representation of steel profiles (black) and wall J2G masonry (brown). (b) Finite element discretization of wall J2G using 2049 elements and 1742 nodes.



**Fig. 11.** Force-displacement curves from experimental results (red line), numerical micro-model analysis (thin blue line), and orthotropic macro-model analysis (thick blue line). The markers (black squares) signal distinctive changes in wall response at  $u_{\rm x}=0.26$  mm (onset of inelastic behavior),  $u_{\rm x}=1.73$  mm (peak force),  $u_{\rm x}=6.93$  mm (onset of residual strength), and  $u_{\rm x}=20.0$  mm (ultimate displacement).

In addition, as an essential validation step, we assess the size effects and mesh sensitivity of the RVEs, as expected during softening responses. In particular, we highlight the role of the adopted regularization scheme, equations (12)–(14), and the use of the stress-displacement curves for computing the effective fracture energy.

#### 4.1. Background

The city of Cuenca has a population of about 300,000 inhabitants [23]. It is located in the southern part of Ecuador, in the Andean Highlands, at about 2350 m to 2550 m above sea level. Cuenca's Historical Center is recognized for its architectural wealth and was added to UN-ESCO's list of World Heritage Trust sites in 1999. In Cuenca, there are more than 60,000 buildings [17]; of these, 43% are confined masonry, 27% are reinforced concrete, 19% are unreinforced masonry, 6% are steel structures, and 3% are timber and other types [11]. Moreover, 80% of the building stock is low-rise, composed of buildings with 1 to 3 stories, from which 53% are two-story dwellings.

Since late 2017, the research group *Vulnerabilidad Sísmica del Patrimonio Edificado de Cuenca* has been studying the seismic vulnerability of Cuenca's buildings in collaboration with the *Red Sísmica del Austro* (seismological observatory and research group in the South of Ecuador). The group aims to increase data and reduce uncertainty by performing experimental compressive tests on units, mortar cubes, and masonry piers.

#### 4.2. Experiments on bricks and mortar

Fig. 14 shows two typical bricks from buildings in Cuenca. The first type is a hollow tochana unit with an average length  $L=30\,\mathrm{cm}$  or 40 cm, height  $h=20\,\mathrm{cm}$ , and width  $b=13\,\mathrm{cm}$ . The second type is a solid burnt unit called panelón, with an average length  $L=28\,\mathrm{cm}$ , height  $h=9\,\mathrm{cm}$ , and width  $b=13\,\mathrm{cm}$ . The experimental compression tests on bricks followed the ASTM C67 standard, while the procedure for mortar adhered to the ASTM C109 standard. The experimental campaign was performed on 144 hollow bricks, 149 sold bricks, and 37 mortar cubes. The mortar composition was 1 part cement, 3 parts sand, and water. This mixture mirrors the one commonly employed by local construction workers during wall assembly. This detail provides context to the present research and underscores its practical application in the local construction industry.

Fig. 15a illustrates the testing equipment just before finalizing a compressive test on a solid brick. The testing equipment is simple and comprises two rigid cylinders, a stationary upper crosshead, and a bottom piston that transmits the load. Table 3 displays the experimental average compressive strength  $f_{\rm c}$  and strain at peak stress  $\epsilon_{\rm p}$  of hollow and

**Table 3** Experimental results from compression tests on hollow and solid bricks of compressive strength  $f_{\rm c}$  at strain  $\epsilon_{\rm p}$ , each result being the average of 10 tests. The bottom section shows the corresponding mean  $\bar{x}$ , standard deviation s, and coefficient of variation

Brick Producer	f <sub>c</sub> [MPa]		$\epsilon_{ m p}$ [-]	
	Hollow	Solid	Hollow	Solid
	1.64	7.72	0.012	0.0027
Sinincay	2.40	8.10	0.011	0.0026
	1.53	8.91	0.013	0.0031
Racar El Tejar	1.82 2.80 1.87 1.80 1.97 1.28	5.72 8.50 5.58 1.71 3.12 4.83	0.007 0.010 0.01 0.003 0.005 0.009	0.0024 0.0029 0.0022 0.0015 0.0018 0.0022
	1.85	6.55	0.008	0.0023
$ar{x}$ $s$ $CV$	1.90 0.43 0.23	6.07 2.37 0.398	0.0088 0.0034 0.39	0.0024 0.0005 0.20

solid bricks obtained from testing units from three manufacturers (mean of 10 tests). The statistical parameters show that solid bricks are more resistant than hollow bricks, with five times higher average compressive strength. A reason for the relatively low strength of hollow bricks lies in the manufacturing process. Most units are handmade, meaning the pieces often have imperfections along the longitudinal voids (Fig. 14a). During the experimental tests, the inner faces of the bricks are expected to crack at relatively low stress, leading to complete failure of the brick.

On the other hand, the compressive tests on mortar cubes yield a mean compressive strength of 7.24 MPa, a median of 7.27 MPa, a standard deviation of 1.17 MPa, and a coefficient of variation of 16.09. For the strain  $\epsilon_{\rm p}$ , the mean is 0.0055, the standard deviation is 0.0012, and the coefficient of variation is 21.8%.

Since experimental testing introduces several sources of uncertainty, it is preferred to fit log-normal probability distribution functions (PDFs). These functions can be fitted using the statistical parameters for bricks and mortar derived from the experimental tests. The PDFs can be used to sample  $f_{\rm c}$  and the corresponding strain  $\epsilon_{\rm p}$  to account for uncertainty due to the variability in the compressive strength and strain of units and mortar.

The fitted log-normal probability distribution functions are used to sample one hundred values of  $f_{\rm c}$  and  $\epsilon_{\rm p}$  for units and mortar. The number of samples is considered sufficient to study the variability. The remaining parameters required for the damage model (section 2) are derived as in subsection 2.2 for the corresponding values of  $f_{\rm c}$  and  $\epsilon_{\rm p}$ . Table 4 presents the derived material properties of the two bricks and the mortar obtained from the average  $f_{\rm c}$  and  $\epsilon_{\rm p}$ .

# 4.3. RVE analyses

Fig. 16 presents the geometry of RVEs composed of hollow (Fig. 16a) and solid (Fig. 16b) bricks. 10 mm quadrilateral elements discretize the domain using 376 and 1729 nodes, and 682 and 945 elements, for hollow bricks and solid bricks respectively. The geometrical characteristics replicate the wall's pattern, i.e., joining RVEs form a typical masonry wall. The element type, boundary conditions, numerical solution under plane stress, and goal of each analysis are the same as in section 3.3.1. We discuss the response of three illustrative RVEs below.

The first analysis concerns the RVE with hollow bricks under tensile loading perpendicular to bed joints. The force-displacement curve in Fig. 17 highlights two distinctive states: the maximum tensile force (4.16 kN) and the force previous to the residual strength (0.40 kN).

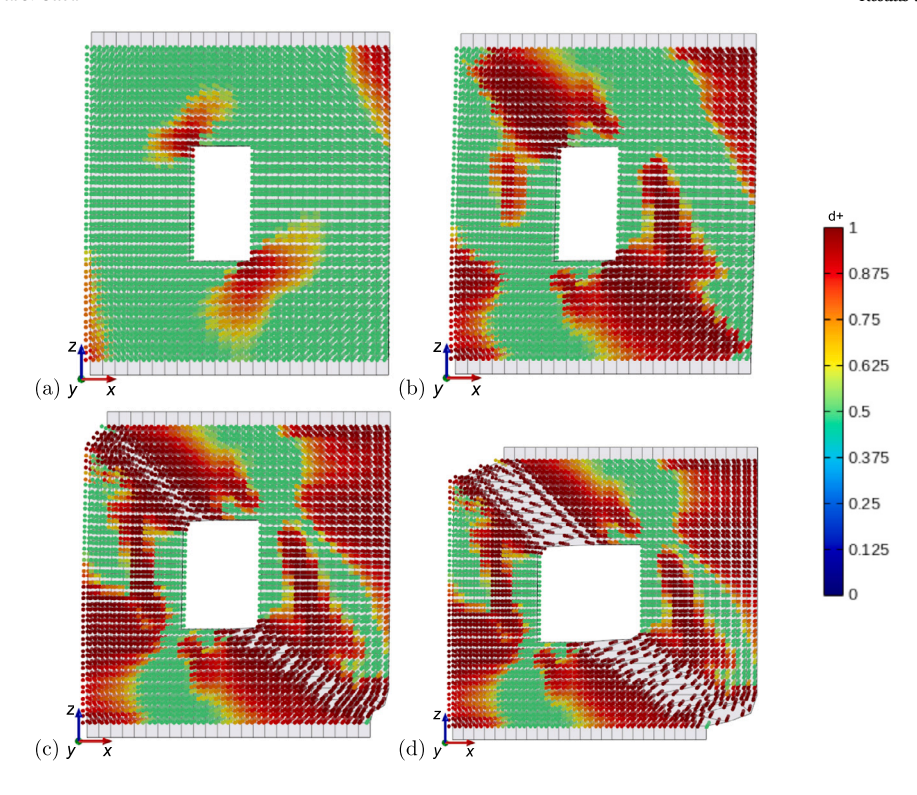
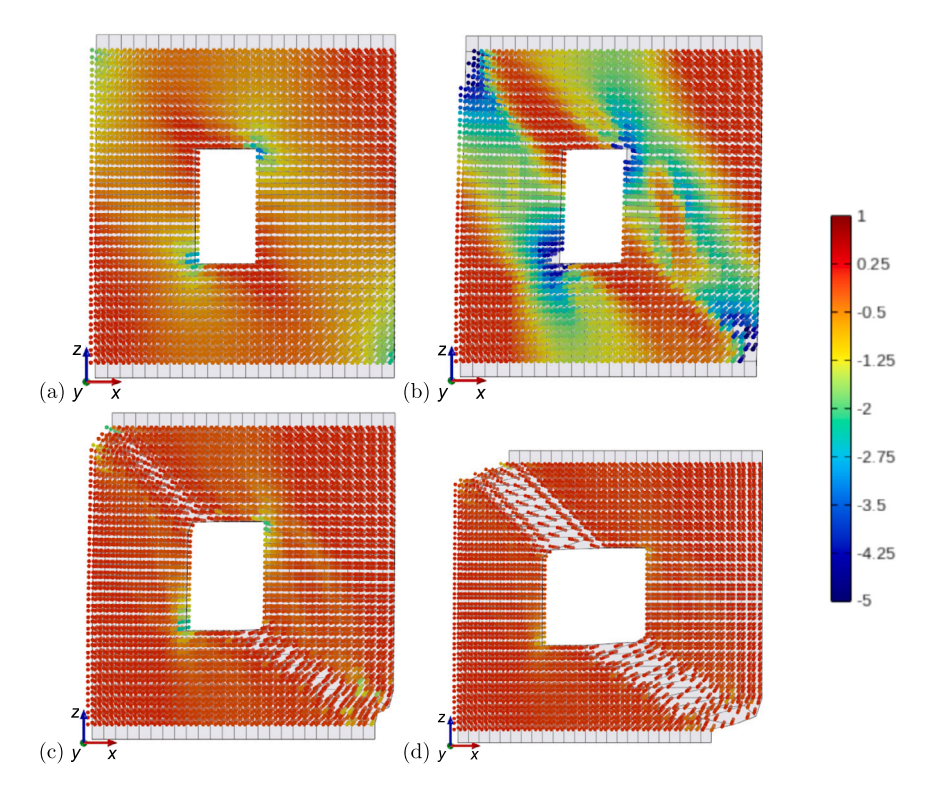


Fig. 12. Tensile damage evolution of wall J2G (color bar) at meaningful points identified by horizontal top-displacements of (a)  $u_x = 0.26$  mm (initiation of inelastic behavior), (b)  $u_x = 1.73$  mm (peak shear force and initiation of softening), (c)  $u_x = 6.93$  mm (initiation of residual strength), and (d)  $u_x = 20.0$  mm (ultimate displacement). The displacement is scaled with a factor of 10.



**Fig. 13.** Minimum principal stress evolution of wall J2G in MPa (color bar) at meaningful points identified by horizontal top-displacements of (a)  $u_x = 0.26$  mm (initiation of inelastic behavior), (b)  $u_x = 1.73$  mm (peak shear force), (c)  $u_x = 6.93$  mm (initiation of softening), and (d)  $u_x = 20.0$  mm (ultimate displacement). The displacement is scaled with a factor of 10.

**Table 4** The material properties of hollow bricks, solid bricks, and mortar defined using average compressive strength  $f_c$  and strain at peak strength  $\epsilon_{\rm p}$ .

Property	Values Hollow bricks	Solid bricks	Mortar	Units
Compressive strength $f_c$	1.9	6.07	7.24	[MPa]
Strain at peak strength $\epsilon_{\mathrm{p}}$	0.0088	0.0024	0.0055	[-]
Young's modulus E	432	5058	2633	[MPa]
Poisson's ratio v	0.18	0.17	0.2	[-]
Tensile strength $f_t$	0.13	0.42	0.51	[MPa]
Tensile fracture energy $G_{\rm t}$	0.004	.012	0.06	[N/mm]
Compressive elastic strength $f_{c0}$	0.63	2.02	2.41	[MPa]
Compressive residual strength $f_r$	0.19	0.61	0.72	[MPa]
Compressive fracture energy $G_{\rm c}$	3.04	9.71	13	[N/mm]



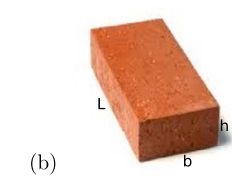


**Fig. 14.** Geometrical parameters: length L, height h, and width b of (a) hollow *tochana* and (b) solid *panelón* bricks used in Cuenca, Ecuador.

Figs. 18 and 19 present the damage states and stresses corresponding to these two points. At tensile strength, damage localizes around the mortar interfaces (Fig. 18a). Immediately after reaching the peak strength, the model presents a quasi-brittle response with increasing damage in the same areas. However, the damage index reaches 1, indicating complete damage in tension. This damage state corresponds to detachment along the mortar joints. Fig. 19a shows the highest tensile stresses at values of 0.2 MPa along the brick-mortar vertical interfaces (top and bottom) and the middle-right side of the RVE. Under increasing load, Fig. 19b shows a state of relaxation due to the failure of most parts of the RVE. However, there are small areas with residual stresses along the horizontal brick-mortar interface.

The second analysis concerns the RVE with solid bricks under compressive loading perpendicular to head joints. Fig. 20 presents the force-displacement curve. In this case, it is possible to identify four distinctive points. The first (159.44 kN) corresponds to the beginning of a strongly inelastic response. Then, the curve shows the maximum strength (200.58 kN) followed by a third point highlighting the loss of stiffness (marked softening). Finally, the fourth point signals the residual strength. Fig. 21 shows the compressive damage at the three latter points. Fig. 21a confirms the onset of a marked non-linear response, with small areas showing minor compressive damage. The maximum strength state (Fig. 21b) shows an increase of damage distributed around the RVE, with higher damage values  $d^-$  for the bricks. Fig. 21c illustrates the damage state under softening behavior. At this stage, the damage around the previous areas increases, reaching values closer to 1. The final state (Fig. 21d), at the onset of residual strength, shows complete failure ( $d^- = 1$ ), consistent with the failure of specimens in compression

Fig. 22a shows higher compressive stresses for the bricks than for the mortar at the onset of a marked inelastic response. The compressive stresses acting on the bricks, conforming most of the RVE, are higher than the mortar since stiffer elements require more load to achieve equal displacement. The compressive stresses along the vertical mortar joints are, on average, 67% lower. The state of stress (Fig. 22b) that results in the maximum strength is characterized by equal compressive stresses transmitted between the bricks. Subsequently, softening is triggered due to damage from a new displacement increment, reducing the stress (Fig. 22c). The final state (Fig. 22d) presents small residual stresses with damage in most elements.

Finally, the third study concerns the RVE with solid bricks under shear loading parallel to the bed joints. Fig. 23 shows the forcedisplacement curve. The model shows an inelastic response at an early stage for a displacement of 0.04 mm. The inelastic stage is characterized by a small stiffness decay with minor tensile damage localized on the bottom-left and top-right corners (Fig. 24a). Moreover, at the onset of a marked inelastic response, the minimum principal stress (Fig. 25a) is positive and relatively small (close to zero). A lateral displacement of 0.17 mm marks the maximum strength. It produces an increase of damage in areas around the compressed diagonal (Fig. 24b), where compressive stresses are higher, reaching values of 6 MPa around the corners (Fig. 25b). Under increasing load, compressive damage spreads, e.g., in the bottom-right corner (Fig. 24c). This damage induces a strainsoftening response and thus a change of behavior, with lower compressive stresses and higher tensile stresses (Fig. 25c). The RVE softens after exceeding a lateral displacement of 0.38 mm. Finally, at a horizontal displacement of 1 mm, damage spreads (Fig. 24d), and compressive stresses reduce (Fig. 25d) along the compressed diagonal. In general, the RVE shows a relatively high strength capacity. This response is characteristic of bearing walls [66] supporting high compressive forces under in-plane lateral loading.

These numerical analyses show results consistent with experimental observations [66]. Tensile failure is characterized by detachment, a typical failure mode for masonry piers subjected to tensile stresses. For the RVE under compressive loading, the results show damage concentrating in the central part of the pier, similar to the damage observed in experimental tests of masonry piers [63]. Finally, the shear analysis characterizes a typical response of masonry piers under lateral and compressive forces [66]. Damage concentrates along the compressed diagonal and (here) the bottom left and right corners.

#### 4.4. Effective properties

Having discussed and validated the response of RVEs with hollow bricks and solid bricks under different loading conditions, we proceed to generate a database of effective properties, considering the variability in material parameters discussed in section 4.2.

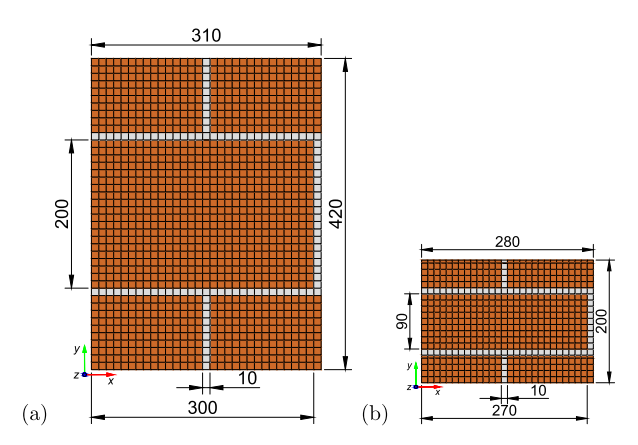
Figs. 26 and 27 show sets of stress-strain curves and force-displacement curves for 100 RVEs with hollow bricks and solid bricks, respectively, due to compressive, tensile, and shear loading. The curves show the results of RVEs with different material properties, derived from compressive strength  $f_{\rm c}$  and strain  $\epsilon_{\rm p}$  values of units and mortar sampled from the fitted log-normal PDFs. As described in section 3.2, at each displacement increment, the stress is computed by averaging the resulting forces and dividing by the corresponding area. Similarly, the strain is determined by averaging the displacement at each increment and dividing by the initial height.

The simulations on RVEs with hollow brick under tensile loading show a brittle material behavior, as expected for this type of material. Additionally, the average tensile strength is significantly lower than the compressive strength, by a factor of  $\sim$ 14. Moreover, we observe that

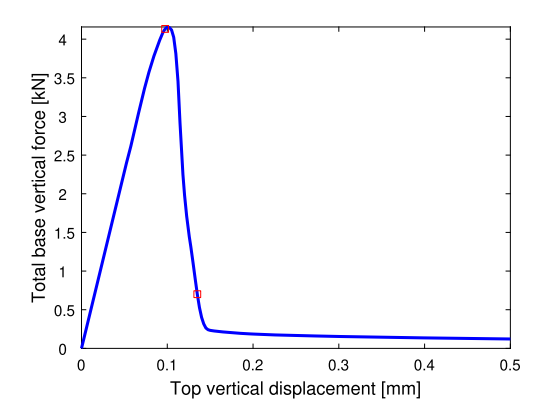




Fig. 15. (a) Experimental setup [40] on a solid brick sample. (b) Pictures of units, mortar, and masonry piers from the second experimental campaign.



**Fig. 16.** The RVEs representing masonry composed of (a) hollow bricks and (b) solid bricks. Superimposed on each figure is the mesh (black borders) representing unit elements (brown fills) and mortar elements (gray fills).



**Fig. 17.** Force-displacement curve due to tensile loading perpendicular to the bed joint of the RVE with hollow bricks. The markers (red squares) correspond to distinctive states at vertical displacements  $u_y = 0.10$  mm (tensile strength) and  $u_v = 0.14$  mm (near-residual strength).

hollow bricks are stronger when compressive loading is applied perpendicular to the head joints compared to the same loading applied perpendicular to the bed joints (Figs. 26a and 26c). However, the simulations show the opposite trend for tensile tests, i.e., bricks are weaker when pulled perpendicular to the head joints.

To verify this result, we conducted experimental tests on two specimens built to characterize these RVEs under compressive loading, applied perpendicular to the bed joints or the head joints (Fig. 28). The average compressive strength of *tochana* bricks from a batch of 50 units is 2.2 MPa, and the average compressive strength from 15 mortar cubes (3 tests per group) is 6.80 MPa. Table 5 summarizes the results from the experimental tests. Higher compressive strength values are observed

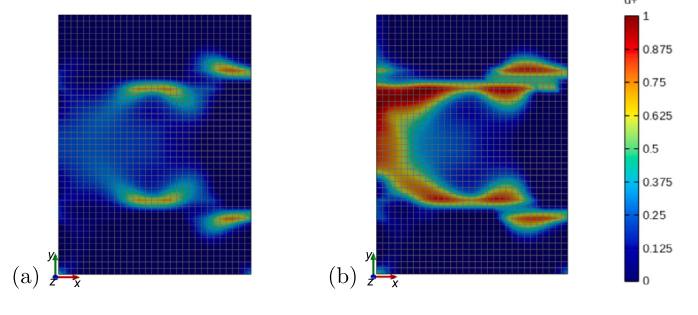


**Fig. 18.** Tensile damage  $d^+$  (color bar) due to tensile loading perpendicular to the bed joint of the RVE with hollow bricks at (a)  $u_y = 0.10$  mm (tensile strength) and (b)  $u_y = 0.14$  mm (near-residual strength).

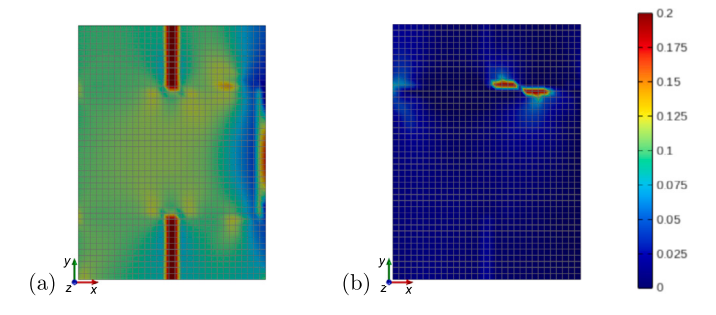


**Fig. 19.** Maximum principal stresses in MPa (color bar) due to tensile loading perpendicular to the bed joint of the RVE with hollow bricks at (a)  $u_y = 0.10$  mm (tensile strength) and (b)  $u_y = 0.14$  mm (near-residual strength).

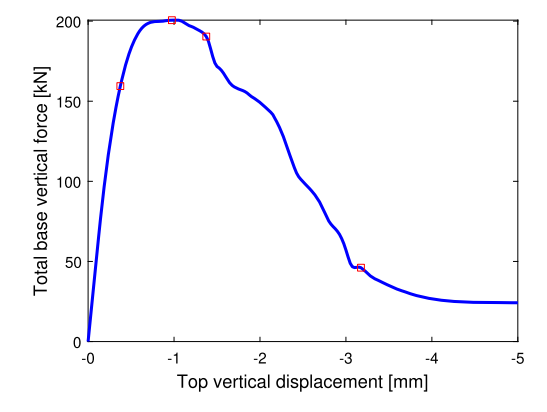


**Fig. 20.** Force-displacement curve due to compressive loading perpendicular to the head joints of the RVE with solid bricks. The markers (red squares) correspond to distinctive states at vertical displacements  $u_y = -0.375$  mm (onset of inelastic behavior),  $u_y = -0.975$  mm (peak strength),  $u_y = -1.375$  mm (onset of softening), and  $u_y = 3.175$  mm (residual strength).

Table 5 Compressive strength  $f_c$ , maximum load  $P_u$ , and gross area A for RVEs of hollow bricks under compressive loading perpendicular to bed joints and head joints. The bottom section shows the corresponding mean  $\bar{x}$ , standard deviation s, and coefficient of variation CV.

	Load perpendicular to bed joint			Load perpendicular to head joint		
Group	f <sub>c</sub> [N/mm^2]	P <sub>u</sub> [N]	A [mm^2]	f <sub>c</sub> [N/mm^2]	<i>P</i> <sub>u</sub> [N]	A [mm^2]
1	0.59	20305.72	34398	1.61	68748.48	42750
2	0.76	26083.81	34510	1.00	43896.81	43957
3	0.73	26448.74	36000	1.10	52966.15	48000
4	0.73	26882.34	36704	1.81	86605.62	47864
5	0.92	32994.95	36000	1.43	69150.69	48440
$\bar{x}$	0.75	26543.11	35522.4	1.39	64273.55	46202.2
S	0.12	4496.28	1017.6	0.34	16474.24	2643.9
CV	0.16	0.17	0.03	0.24	0.26	0.06

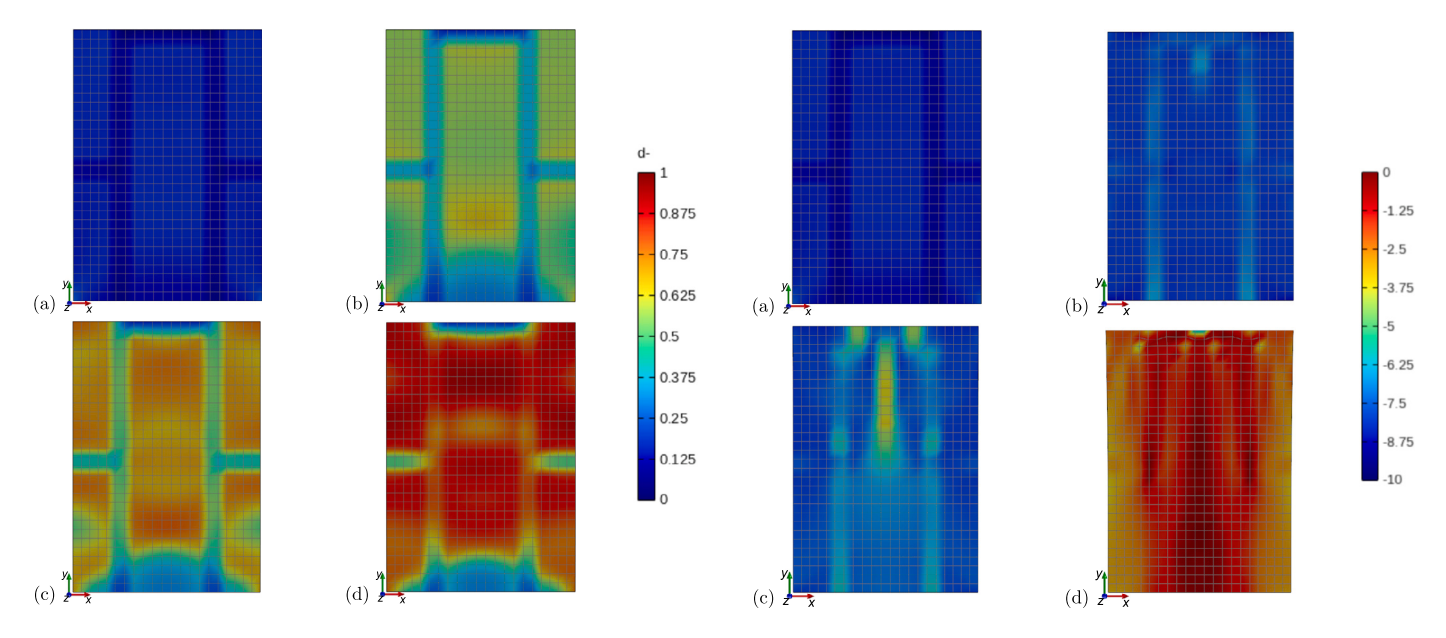


**Fig. 21.** Compressive damage  $d^-$  (color bar) due to compressive loading perpendicular to the head joints of the RVE with solid bricks at (a)  $u_y=0.40\,$  mm (inelastic behavior), (b)  $u_y=1.00\,$  mm (compressive strength), (c)  $u_y=1.40\,$  mm (softening), and (d)  $u_y=3.20\,$  mm (residual strength).

**Fig. 22.** Minimum principal stresses in MPa (color bar) due to compressive loading perpendicular to the head joints of the RVE with solid bricks at (a)  $u_y = 0.40$  mm (inelastic behavior), (b)  $u_y = 1.00$  mm (compressive strength), (c)  $u_y = 1.40$  mm (softening), and (d)  $u_y = 3.20$  mm (residual strength).

for the RVE under compressive forces perpendicular to the head joints, agreeing with the numerical results.

The difference in strength can be due to the variation in position, length, and material characteristics of the mortar elements, which are stiffer than hollow brick elements. For instance, in the RVEs under compression perpendicular to head joints, the mortar elements bear the forces from top to bottom. In the case of tensile loading, the strength highly depends on the contact area, a function of the total length of the mortar elements. Under loading perpendicular to bed joints and head joints, the mortar layer has a length of 310 mm and 200 mm, respectively.

The curves from compressive and tensile analysis on RVEs with solid bricks show a slight difference in strength between the two configurations. In this case, bricks are stiffer than mortar, reducing the effect of mortar position and length on the composite strength. Nevertheless, there is still a slight difference. Under compression, Fig. 27a shows a mean compressive strength of 5.75 MPa, while the mean curve from Fig. 27c shows a maximum strength of 5.36 MPa. For tensile loading, the results are the opposite. The mean curve resulting from forces perpendicular to the bed joints shows an ultimate tensile strength of 0.37 MPa, while in the other case, the mean tensile strength is 0.41 MPa.

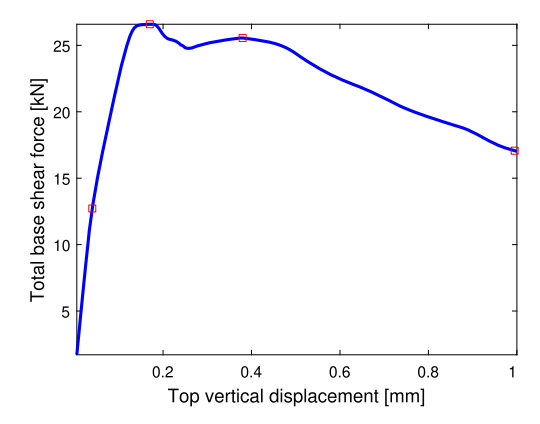


**Fig. 23.** Force-displacement curve due to shear loading parallel to the bed joints of the RVE with solid bricks. The markers (red squares) correspond to distinctive states at imposed horizontal displacements  $u_{\rm x}=0.04$  mm (onset of inelastic behavior),  $u_{\rm x}=0.17$  mm (peak strength),  $u_{\rm y}=0.38$  mm (onset of softening), and  $u_{\rm y}=1$  mm (residual strength).

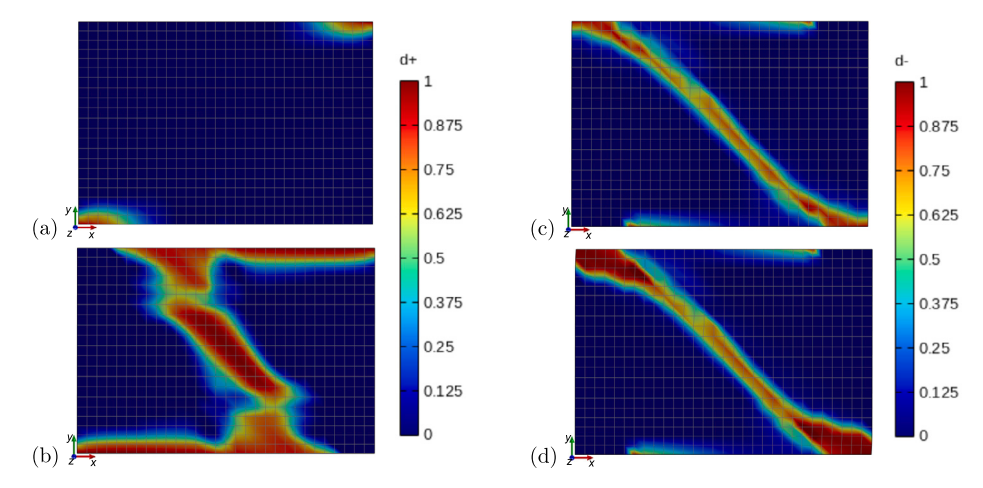


Fig. 24. Tensile damage  $d^+$  and compressive damage  $d^-$  due to shear loading parallel to the bed joints of the RVE with solid bricks at (a)  $u_x = 0.04$  mm (onset of inelastic behavior), (b)  $u_x = 0.17$  mm (peak strength) (c)  $u_x = 0.38$  mm (softening), and (d)  $u_x = 1.00$  mm (residual strength).

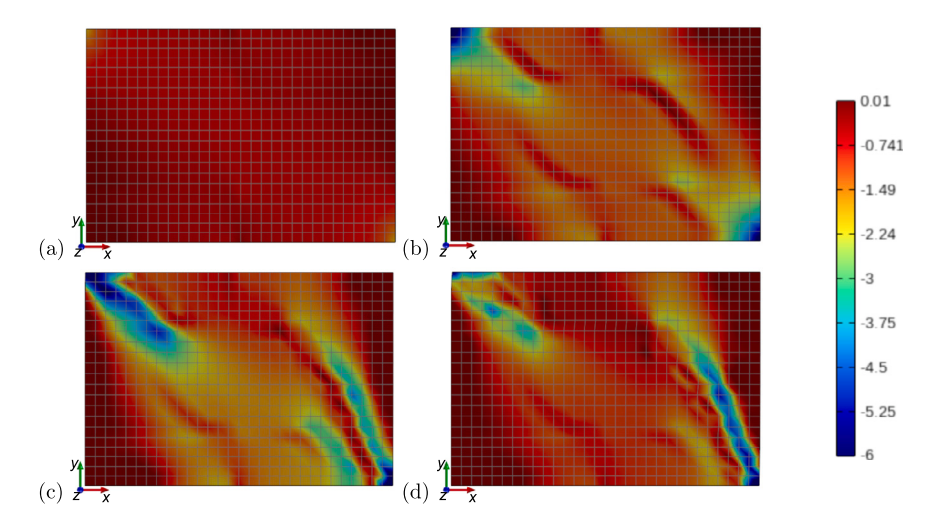


Fig. 25. Minimum principal stresses in MPa (color bar) due to shear loading parallel to the bed joints of the RVE with solid bricks at (a)  $u_x = 0.04$  mm (onset of inelastic behavior), (b)  $u_x = 0.17$  mm (compressive strength), (c)  $u_x = 0.38$  mm (softening), and (d)  $u_x = 1.00$  mm (residual strength).

Table 6 presents the effective material properties for the damage model resulting from the multiple analyses. This database contributes toward characterizing masonry buildings using a macro-element approach. In particular, the damage model informed by effective properties can improve the characterization of masonry for the seismic assessment of masonry buildings, as typical in the city of Cuenca. In this sense, progress has been made in defining a catalog of typical buildings from Cuenca's historical center [60].

#### 4.5. Size effects and mesh sensitivity

In the previous sections, the curves resulting from numerical analyses on RVEs were used to obtain effective masonry properties in two in-plane directions. These properties characterized the damage model at the macro-scale level [58], yielding accurate and representative results.

However, it is crucial to assess the reliability of this numerical framework, in particular, concerning size effects and mesh sensitivity in the finite element simulations during softening. The objective is to ensure that the derived material properties remain relatively consistent, regardless of the model's size or mesh discretization. This consistency is essential for validating the procedure. To this end, we compare results across specimens of different sizes, considering systems composed of

1 RVE, 4 RVEs, and 16 RVEs under compressive and tensile loading (Fig. 29). We conduct simulations under applied displacements up to 5 mm for compression and 0.25 mm for tension. The boundary conditions and numerical procedure are the same as in subsection 4.3.

Fig. 30 shows stress-strain and stress-displacement curves for the three specimens under compressive and tensile loading. All cases yield the same Young's modulus and compressive strength from the stress-strain curves in compression. However, the post-peak response varies across specimens. In particular, smaller specimens show a higher degree of toughness as expected. Conversely, the stress-displacement curves present stiffness variation, with higher stiffness for the smaller specimens. The tensile test results exhibit similar behavior: the stress-strain curves show the same Young's modulus and small variations in tensile strength (~3% higher for the smaller samples), while the stress-displacement curves show higher stiffness for smaller specimens. However, in both analyses, the lower stiffness in the stress-displacement curves is accompanied by much larger displacements at the same stress level in the post-peak stage. As a result, the area under the curve, characterizing the fracture energy, is similar for the three specimens.

Table 7 summarizes five key material properties that characterize the damage model in the linear, inelastic, and softening stages. The differences in fracture energy between the models are reasonable ( $\sim$ 13%

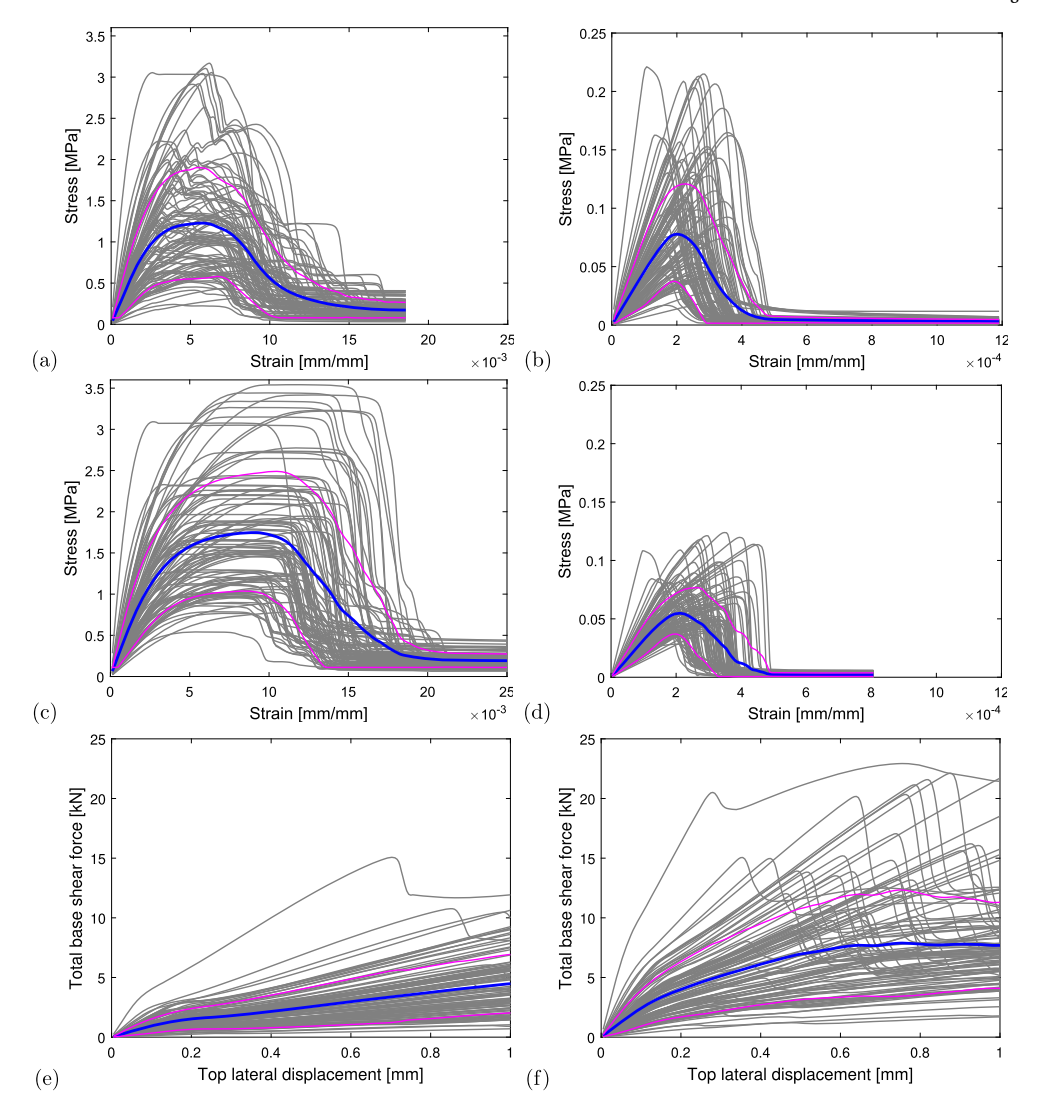


Fig. 26. Stress-strain curves from 100 RVEs of hollow bricks (gray) under distributed loads perpendicular to bed joints for (a) compression and (b) tension, and perpendicular to head joints for (c) compression and (d) tension. Force-displacement curves for shear loading (e) parallel to bed joints and (f) parallel to head joints. Superimposed on each figure are the mean (blue) and the mean plus/minus one standard deviation (magenta). The curves correspond to RVEs with different material properties, derived from compressive strength and strain values of units and mortar sampled from the fitted log-normal PDFs.

for compressive fracture energy and >10% for tensile fracture energy), lower than the coefficient of variation of the energy parameters obtained from the numerical analyses.

Nevertheless, the difference is likely due to different failure modes triggered in larger samples. Fig. 31 shows the final fracture state of the three specimens in compression at the target displacement (5 mm). The fracture energy per unit area of the first two specimens (Figs. 31a and 31b) is approximately the same. The model with 16 RVEs presents a slight increase in fracture energy per unit area due to a vertical crack (Fig. 31c). On the other hand, for tensile loading, we can observe from Fig. 32 that the fracture modes are similar for all three cases, with cracks developing in the lower section.

Finally, Fig. 30b and Fig. 30d assess the effect of mesh discretization, showing results for element sizes of 1 mm, 10 mm, and 15 mm. The results are indistinguishable up to the peak and show slight variation in the softening stage. Signs of convergence are seen when comparing results across different mesh sizes: discrepancies are smaller between the 1 mm and 10 mm meshes than between 10 mm and 15 mm. This trend suggests that the results progressively converge towards a stable solution as the mesh size decreases.

These results highlight promising aspects of the present framework. The composite maximum strengths are objectively captured and can therefore be well estimated, including the tensile strength, which is commonly a critical parameter for failure analysis, further influencing the wall's shear capacity. Consequently, the results suggest that the properties obtained from analyzing small samples (one or a few RVEs) may provide reasonable approximations of the effective properties of the continuum material. Moreover, since one RVE represents a relatively small model, it is possible to use a fine discretization with limited computational cost.

#### 5. Conclusion

We have presented a simple framework for determining effective masonry properties, for use in macro-model structural simulations. It was shown that these properties may be estimated in a relatively simple manner, without resorting to rigorous homogenization methods. Specifically, a damage model was used to conduct direct numerical simulations on RVEs, including a practical procedure for defining the base material properties from experimental tests on units and mortar. The micro-model results were then used to derive the effective properties re-

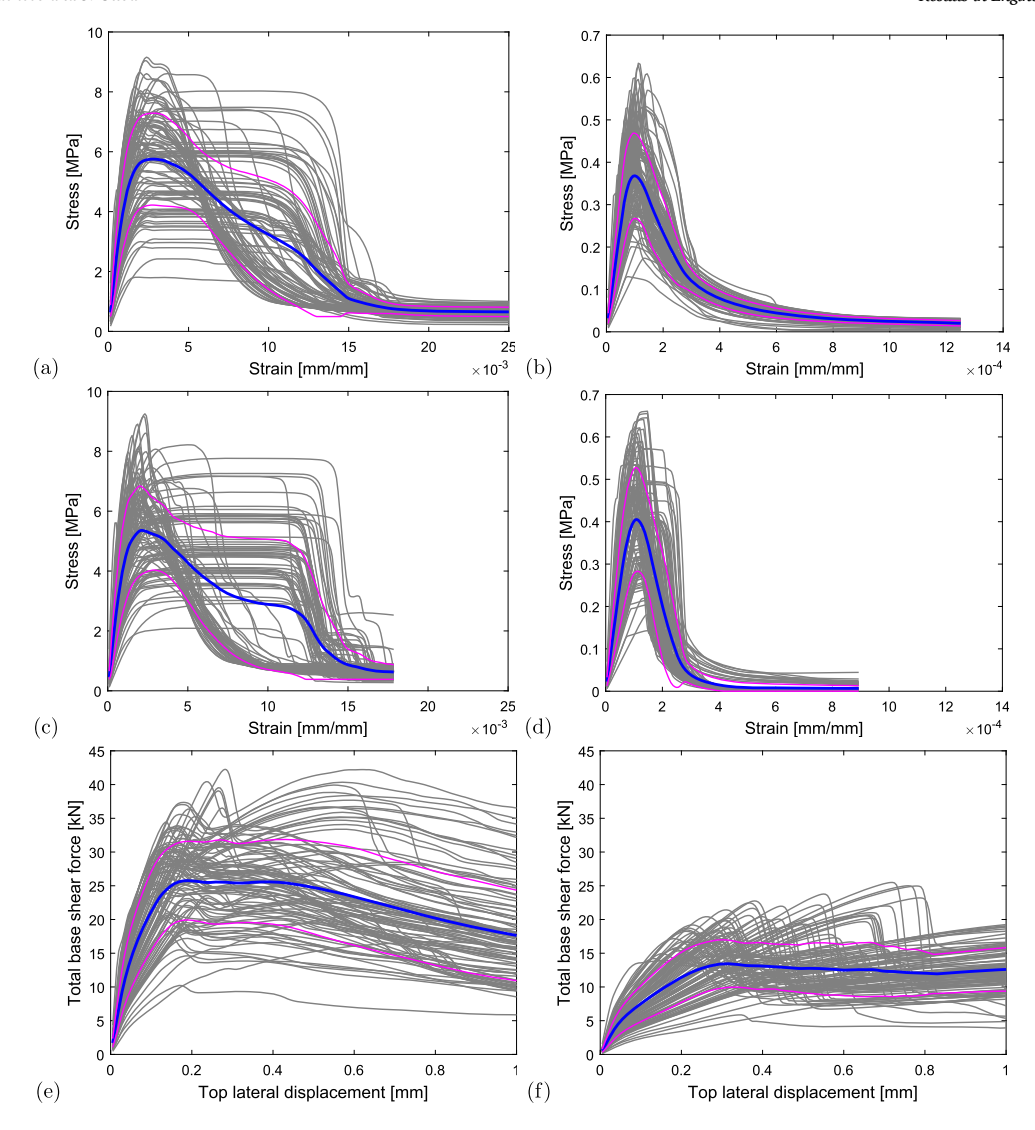


Fig. 27. Stress-strain curves from 100 RVEs of solid bricks (gray) under distributed loads perpendicular to bed joints for (a) compression and (b) tension, and perpendicular to head joints for (c) compression and (d) tension. Force-displacement curves for shear loading (e) parallel to bed joints and (f) parallel to head joints. Superimposed on each figure are the mean (blue) and the mean plus/minus one standard deviation (magenta). The curves correspond to RVEs with different material properties, derived from compressive strength and strain values of units and mortar sampled from the fitted log-normal PDFs.

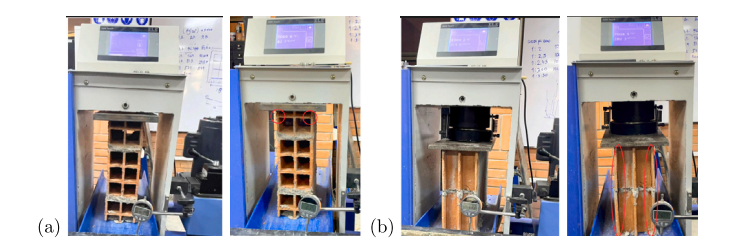


Fig. 28. RVEs of hollow bricks prior to and after being tested under compressive loading perpendicular (a) to bed joints and (b) to head joints.

quired for the macro-model directly. Using both stress-strain and stress-displacement curves was crucial to alleviate the size dependence of the effective parameters, particularly concerning fracture energy. Moreover, a conventional fracture energy-based regularization method proved effective in preventing mesh sensitivity. The analyses are performed in two directions, accounting for orthotropic behavior, which was shown to be essential for reproducing experimental observations.

The validation of the macro-model informed by the derived effective properties showed accurate predictions of the global response, kinematics, stresses, and damage states, consistent with direct micro-modeling results and experimental observations of masonry walls. Furthermore, the present framework was applied to compute the effective properties of two types of masonry walls, typical of masonry buildings in Cuenca, Ecuador. The resulting properties comprise a database that may be used for future regional investigations.

The present study contributes to the calibration of macro-models for accurate characterizations of masonry walls. The methodology, being simple to apply, can adapt to the modeling of masonry in 3D structures for design and assessment. One limitation is that the damage model requires several material parameters. Additionally, the material properties were derived from empirical relations, not experimental testing. Finally, the proposed methodology lacks a theoretical background; thus, it is not shown to be valid for boundary and loading conditions beyond the present analyses. Further research is therefore required for more complex walls under different loading conditions. It would also be interesting to compare the present framework with other, perhaps rigorous, homogenization methods. Additional experimental testing is also nec-

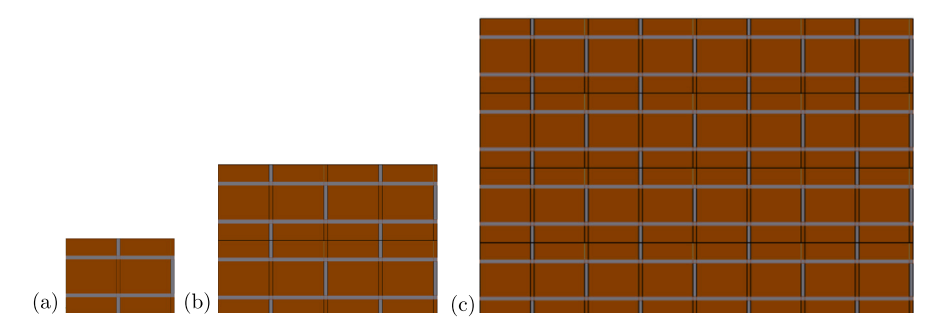


Fig. 29. Masonry piers with solid bricks composed of (a) 1 RVE, (b) 4 RVEs, and (c) 16 RVEs.

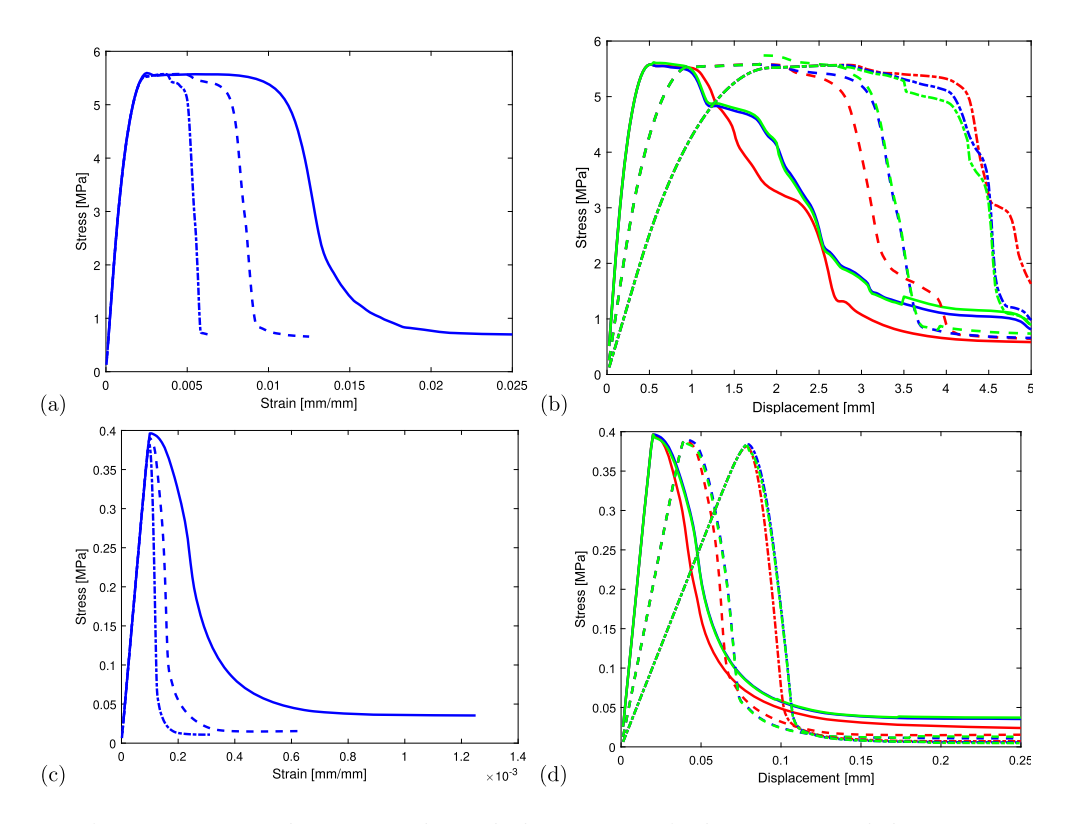


Fig. 30. Stress-strain curves for (a) compression and (c) tension and stress-displacement curves for (b) compression and (d) tension on 1 RVE (solid blue lines), 4 RVEs (dashed blue lines), and 16 RVEs (dash-dot blue lines), discretized with a mesh size of 10 mm. The results of using a mesh size of 1 mm (green lines) and 15 mm (red lines) are superimposed on the stress-displacement curves.

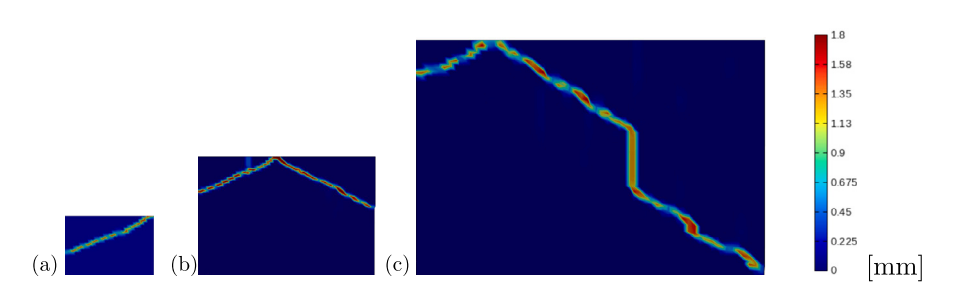


Fig. 31. Failure pattern in compression at an imposed displacement of 5 mm on (a) 1 RVE, (b) 4 RVEs, and (c) 16 RVEs representing masonry piers with solid bricks and an element size of 10 mm.

Table 6
Mean  $\bar{x}$  star

Mean  $\bar{x}$ , standard deviation s, and coefficient of variation CV of effective properties for masonry obtained from compression, tensile, and shear analyses on RVEs: Young's modulus  $\bar{E}$ , shear modulus  $\bar{G}$ , tensile strength  $\bar{f}_{\rm c}$ , tensile fracture energy  $\bar{G}_{\rm t}$ , compressive elastic strength  $\bar{f}_{\rm c0}$ , compressive strength  $\bar{f}_{\rm c}$ , compressive residual strength  $\bar{f}_{\rm r}$ , compressive fracture energy  $\bar{G}_{\rm c}$  and strain at peak strength  $\bar{e}_{\rm p}$ .

Ē [MPa]	$ar{G}$ [MPa]	$ar{f_{ m t}}$ [MPa]	$ar{G}_{ m t}$ [N/mm]	$ar{f}_{ m c0}$ [MPa]	$ar{f_{ m c}}$ [MPa]	$ar{f_{ m r}}$ [MPa]	$ar{G}_{ m c}$ [N/mm]	$ar{\epsilon}_{ m p}$ [-]
DVEc v di	irection (holl	ow bricks)						
460.58	93.57	0.096	0.0023	0.656	1.328	0.226	2.834	0.0056
297.95	64.97	0.05	0.0023	0.52	0.71	0.13	1.65	0.0030
0.65	0.69	0.53	0.66	0.80	0.54	0.55	0.58	0.36
RVEs x di	irection (hol	low bricks)						
514.66	133.23	0.068	0.0009	0.48	1.770	0.260	3.56	0.008
283.73	92.03	0.02	0.00	0.28	0.72	0.10	2.01	0.003
0.55	0.69	0.34	0.47	0.58	0.41	0.38	0.57	0.302
RVEs y di	irection (soli	d bricks)						
5086.0	1620.2	0.42	0.015	2.42	5.90	1.16	9.04	0.002
1933.8	617.6	0.11	0.002	0.75	1.61	0.31	2.20	0.001
0.4	0.4	0.27	0.166	0.31	0.27	0.27	0.24	0.57
RVEs x di	irection (soli	d bricks)						
5093	1029	0.42	0.009	2.35	5.92	1.13	8.73	0.004
2258	424	0.12	0.003	0.82	1.57	0.37	2.52	0.002
0.4	0.4	0.29	0.383	0.35	0.27	0.32	0.29	0.57

**Table 7** Effective properties: Young's modulus  $\bar{E}$ , compressive strength  $\bar{f}_{\rm c}$ , tensile strength  $\bar{f}_{\rm t}$ , compressive fracture energy  $\bar{G}_{\rm c}$ , and tensile fracture energy  $\bar{G}_{\rm t}$ , resulting from compressive and tensile analyses on 1 RVE, 4 RVEs, and 16 RVEs representing masonry piers with solid bricks. The first three rows present the results of RVEs with an element size of 10 mm, while the last three rows present the

results of RVEs with an element size of 15 mm.

# RVEs	Ē [MPa]	$ar{f_{ m c}}$ [MPa]	$ar{f_{ m t}}$ [MPa]	$ar{G}_{ m c}$ [N/mm]	$ar{G}_{ m t}$ [N/mm]
1	4098	5.59	0.396	13.7	0.02
4	4098	5.57	0.390	13.8	0.018
16	4098	5.57	0.382	16.0	0.02
1	4098	5.59	0.396	11.7	0.015
4	4098	5.57	0.390	13.5	0.017
16	4098	5.57	0.382	17.0	0.019

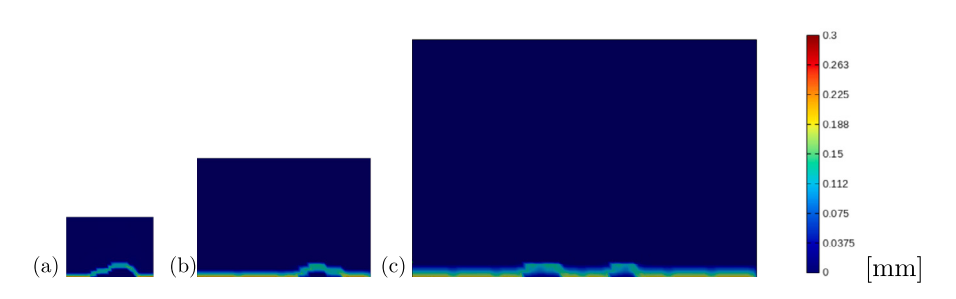


Fig. 32. Failure pattern in tension at an imposed displacement of 0.25 mm on (a) 1 RVE, (b) 4 RVEs, and (c) 16 RVEs representing masonry piers with solid bricks and an element size of 10 mm.

essary to improve the calibration of numerical models concerning the fracture energy parameters, the shear-compression reduction, and the compressive bi-axial strength factors (here, the latter two parameters were assumed from the literature according to the type of units and mortar). Studying other possible brick configurations, such as interlocking units [39], is also worth considering.

#### CRediT authorship contribution statement

Hernán García: Writing – original draft, Validation, Methodology, Investigation, Conceptualization. Juan Jiménez-Pacheco: Writing – review & editing. Jacinto Ulloa: Writing – review & editing, Conceptualization.

#### **Declaration of competing interest**

The authors declare that they have no known competing financial interests or personal relationships that could have appeared to influence the work reported in this paper.

#### Data availability

Data will be made available on request.

#### References

- [1] N. Ahmad, H. Crowley, R. Pinho, Q. Ali, Frame-elements constitutive law for nonlinear static and dynamic analyses of masonry buildings, in: Modern Methods and Advances in Structural Engineering and Construction, 2011.
- [2] M. Angelillo, P.B. Lourenço, G. Milani, Masonry behaviour and modelling, in: Mechanics of Masonry Structures, Springer, 2014, pp. 1–26.
- [3] C. Baggio, P. Trovalusci, Limit analysis for no-tension and frictional threedimensional discrete systems, J. Struct. Mech. 26 (3) (1998) 287–304.
- [4] Z.P. Bažant, B.H. Oh, Crack band theory for fracture of concrete, Mater. Struct. 16 (3)
- [5] A. Benedetti, L. Pelà, A. Aprile, Masonry properties determination via splitting tests on cores with a rotated mortar layer, in: Proceedings of 8th International Seminar on Structural Masonry, Istanbul, Turkey, 2008.
- [6] J. Betten, Creep theory of anisotropic solids, J. Rheol. 25 (6) (1981) 565-581.
- [7] J. Betten, Applications of tensor functions to the formulation of yield criteria for anisotropic materials, Int. J. Plast. 4 (1) (1988) 29–46.
- [8] G. Camata, C. Marano, V. Sepe, E. Spacone, R. Siano, M. Petracca, P. Roca, L. Pelà, Validation of non-linear equivalent-frame models for irregular masonry walls, Eng. Struct. 253 (2022) 113755.
- [9] M. Cervera, M. Chiumenti, Mesh objective tensile cracking via a local continuum damage model and a crack tracking technique, Comput. Methods Appl. Mech. Eng. 196 (1–3) (2006) 304–320.
- [10] M. Cervera, J. Oliver, R. Faria, Seismic evaluation of concrete dams via continuum damage models, Earthq. Eng. Struct. Dyn. 24 (9) (1995) 1225–1245.
- [11] E. Cornejo, J. Zuñiga, Caracterización del patrimonio edificado irregular de baja altura del Centro Histórico de Cuenca, orientado a estudios de vulnerabilidad sísmica, Master's thesis, University of Cuenca, 2019.
- [12] A.M. D'Altri, S. de Miranda, G. Castellazzi, V. Sarhosis, A 3d detailed micro-model for the in-plane and out-of-plane numerical analysis of masonry panels, Comput. Struct. 206 (2018) 18–30.
- [13] K. Dolatshahi, A. Aref, Two-dimensional computational framework of meso-scale rigid and line interface elements for masonry structures, Eng. Struct. 33 (12) (2011) 3657–3667.
- [14] M. Dutko, D. Perić, D.R.J. Owen, Universal anisotropic yield criterion based on superquadric functional representation: part 1. algorithmic issues and accuracy analysis, Comput. Methods Appl. Mech. Eng. 109 (1–2) (1993) 73–93.
- [15] A. D'Altri, V. Sarhosis, G. Milani, J. Rots, S. Cattari, S. Lagomarsino, E. Sacco, A. Tralli, G. Castellazzi, S. de Miranda, Modeling strategies for the computational analysis of unreinforced masonry structures: review and classification, Arch. Comput. Methods Eng. 27 (2020) 1153–1185.
- [16] R. Faria, J. Oliver, M. Cervera, A strain-based plastic viscous-damage model for massive concrete structures, Int. J. Solids Struct. 35 (14) (1998) 1533–1558.
- [17] G.A.D. Cuenca, Cambio climático, riesgos naturales y crecimiento urbano en ciudades emergentes y sostenibles: Estudio urbano Cuenca, Tech. Rep., GAD Cuenca,
- [18] D. Gaetano, F. Greco, L. Leonetti, P. Lonetti, A. Pascuzzo, C. Ronchei, An interface-based detailed micro-model for the failure simulation of masonry structures, Eng. Fail. Anal. 142 (2022) 106753.
- [19] R. Hill, A theory of the yielding and plastic flow of anisotropic metals, Proc. R. Soc. Lond. Ser. A, Math. Phys. Sci. 193 (1033) (1948) 281–297.

- [20] R. Hill, The Mathematical Theory of Plasticity, vol. 11, Oxford University Press, 1998
- [21] O. Hoffman, The brittle strength of orthotropic materials, J. Compos. Mater. 1 (2) (1967) 200–206.
- [22] Y. Hua, G. Milani, Simple modeling of reinforced masonry arches for associated and non-associated heterogeneous limit analysis, Comput. Struct. 280 (2023) 106987.
- [23] INEC, Resultados del censo 2010 de población y vivienda: Fascículo provincial Azuay, Tech. Rep., INEC, 2020.
- [24] S. Lagomarsino, S. Cattari, Non-linear seismic analysis of masonry buildings by the equivalent frame model, in: Proceedings of 11th DA-CH Conference, 2009, pp. 10–11.
- [25] P.B. Lourenço, Computational strategies for masonry structures, PhD thesis, TU Delft, 1996
- [26] P.B. Lourenço, G. Milani, A. Tralli, A. Zucchini, Analysis of masonry structures: review of and recent trends in homogenization techniques, Can. J. Civ. Eng. 34 (11) (2007) 1443–1457.
- [27] P.B Lourenço, P. Roca, C. Modena, S. Agrawal, G. Martinez, O. Caselles, J. Clapés, Characterization of the dynamic response for the structure of Mallorca Cathedral, in: Proceedings of Structural Analysis of Historical Constructions, 2006.
- [28] P.B. Lourenço, Challenges on computational strategies for masonry structures: homogenization techniques and seismic analysis, in: Proceedings of the 10th HSTAM International Congress on Mechanics, 2013.
- [29] P.B. Lourenço, P.B. Almeida, J. Barros, Experimental investigation of bricks under uniaxial tensile testing, Mason. Int. 18 (1) (2005) 11–20.
- [30] P.B. Lourenço, G. Milani, Masonry behavior of regularly arranged masonry structures. homogenization and refined models, in: Mechanics of Masonry Structures, Springer, 2014, pp. 13–26.
- [31] X. Lu, Y. Tian, S. Cen, H. Guan, L. Xie, L. Wang, A high-performance quadrilateral flat shell element for seismic collapse simulation of tall buildings and its implementation in OpenSees, J. Earthq. Eng. 22 (9) (2018) 1662–1682.
- [32] J. Lubliner, J. Oliver, S. Oller, E. Oñate, A plastic-damage model for concrete, Int. J. Solids Struct. 25 (3) (1989) 299–326.
- [33] R. Luciano, E. Sacco, Homogenization technique and damage model for old masonry material, Int. J. Solids Struct. 34 (24) (1997) 3191–3208.
- [34] G. Magenes, M. Remino, C. Manzini, P. Morandi, D. Bolognini, Sam II, Software for the Simplified Seismic Analysis of Masonry Buildings, University of Pavia and EUCENTRE, 2006.
- [35] V. Mallardo, R. Malvezzi, E. Milani, G. Milani, Seismic vulnerability of historical masonry buildings: a case study in Ferrara, J. Eng. Struct. 30 (8) (2008) 2223–2241.
- [36] R. Marques, P.B. Lourenço, A model for pushover analysis of confined masonry structures: implementation and validation, Bull. Earthq. Eng. 11 (6) (2013) 2133–2150.
- [37] T.J. Massart, R.H.J. Peerlings, M. Geers, An enhanced multi-scale approach for masonry wall computations with localization of damage, Int. J. Numer. Methods Eng. 69 (5) (2007) 1022–1059.
- [38] W.S. McNary, D.P. Abrams, Mechanics of masonry in compression, J. Struct. Eng. 111 (4) (1985) 857–870.
- [39] M. Nadeem, A. Gul, A. Bahrami, M. Azab, S.W. Khan, K. Shahzada, Evaluation of mechanical properties of cored interlocking blocks—a step toward affordable masonry material, Results Eng. 18 (2023) 101128.
- [40] F. Neira, L. Ojeda, Dinteles de ladrillo armado, Master's thesis, University of Cuenca, 1992.
- [41] V. Nguyen, M. Stroeven, L. Sluys, Multiscale continuous and discontinuous modeling of heterogeneous materials: a review on recent developments, J. Multiscale Model. 3 (04) (2011) 229–270.
- [42] J.M. Nichols, Y.Z. Totoev, Experimental determination of the dynamic Modulus of Elasticity of masonry units, in: Proceedings of the 11th International Brick and Block Masonry Conference, Shanghai, China, 1997.
- [43] J. Oliver, A consistent characteristic length for smeared cracking models, Int. J. Numer. Methods Eng. 28 (2) (1989) 461–474.
- [44] J. Oliver, A.E. Huespe, J.C. Cante, An implicit/explicit integration scheme to increase computability of non-linear material and contact/friction problems, Comput. Methods Appl. Mech. Eng. 197 (21–24) (2008) 1865–1889.
- [45] S. Oller, S. Botello, J. Miquel, E. Oñate, An anisotropic elastoplastic model based on an isotropic formulation, Eng. Comput. 12 (3) (1995) 245–262.
- [46] S. Oller, E. Car, J. Lubliner, Definition of a general implicit orthotropic yield criterion, Comput. Methods Appl. Mech. Eng. 192 (7–8) (2003) 895–912.
- [47] A.W. Page, The biaxial compressive strength of brick masonry, Proc., Inst. Civ. Eng. 3 (1981) 893–906.
- [48] G.N. Pande, J.X. Liang, J. Middleton, Equivalent elastic moduli for brick masonry, Comput. Geotech. 8 (3) (1989) 243–265.
- [49] B. Pantò, F. Cannizzaro, I. Caliò, P.B. Lourenço, Numerical and experimental validation of a 3D macro-model for the in-plane and out-of-plane behavior of unreinforced masonry walls, Int. J. Arch. Heritage 11 (7) (2017) 946–964.
- [50] L. Pelà, M. Cervera, P. Roca, Continuum damage model for orthotropic materials: application to masonry, Comput. Methods Appl. Mech. Eng. 200 (9–12) (2011) 917–930.
- [51] L. Pelà, M. Cervera, P. Roca, An orthotropic damage model for the analysis of masonry structures, Constr. Build. Mater. 41 (2013) 957–967.
- [52] L. Pelà, Continuum damage model for nonlinear analysis of masonry structures, PhD thesis, Universitat Politècnica de Catalunya, 2009.

- [53] M. Pepe, M. Pingaro, P. Trovalusci, E. Reccia, L. Leonetti, Micromodels for the inplane failure analysis of masonry walls: limit analysis, fem and fem/dem approaches, Frattura Integr. Strutt. 14 (51) (2020) 504–516.
- [54] M. Petracca, Computational Multiscale Analysis of Masonry Structures, type, Universitat Politècnica de Catalunva. 2016.
- [55] M. Petracca, F. Candeloro, G. Camata, STKO user manual, 2017.
- [56] M. Petracca, L. Pelà, R. Rossi, S. Oller, G. Camata, E. Spacone, Regularization of first order computational homogenization for multiscale analysis of masonry structures, Comput. Mech. 57 (2) (2016) 257–276.
- [57] M. Petracca, L. Pelà, R. Rossi, S. Oller, G. Camata, E. Spacone, Multiscale computational first order homogenization of thick shells for the analysis of out-of-plane loaded masonry walls, Comput. Methods Appl. Mech. Eng. 315 (2017) 273–301.
- [58] M. Petracca, L. Pelà, R. Rossi, S. Zaghi, G. Camata, E. Spacone, Micro-scale continuous and discrete numerical models for nonlinear analysis of masonry shear walls, Constr. Build. Mater. 149 (2017) 296–314.
- [59] F. Portioli, C. Casapulla, M. Gilbert, L. Cascini, Limit analysis of 3d masonry block structures with non-associative frictional joints using cone programming, Comput. Struct. 143 (2014) 108–121.
- [60] A. Quezada, J. Jiménez, J. Calderón, H. García, Characterization of the built heritage, oriented to studies of seismic vulnerability at territorial scale: case study Historic Centre of Cuenca, Ecuador, in: Construction Pathology, Rehabilitation Technology and Heritage Management, Granada, Spain, 2020.
- [61] T.M.J. Raijmakers, A. Vermeltfoort, Deformation controlled tests in masonry shear walls, Tech. Rep., TU Delft, the Netherlands, 1992.
- [62] J. Rots, Structural Masonry: an Experimental/Numerical Basis for Practical Design Rules, Tech. Rep. 171, CRC Press, 1997 (in Dutch).

- [63] P. Schubert, Compressive and tensile strength of masonry, in: 8th International Brick and Block Masonry Conference, Dublin, Irland, 1998.
- [64] P. Schubert, Influence of mortar on the strength of masonry, in: 8th International Brick and Block Masonry Conference, Dublin, Irland, 1998.
- [65] M. Scott, G. Fenves, Krylov subspace accelerated Newton algorithm: application to dynamic progressive collapse simulation of frames, J. Struct. Eng. 136 (5) (2010) 473-480
- [66] M. Tomaževič, R. Velochovsky, Some aspects of experimental testing of seismic behavior of masonry walls and models of masonry buildings, ISET J. Earthq. Technol. 37 (4) (2000) 101–117
- [67] S. Tsai, E. Wu, A general theory of strength for anisotropic materials, J. Compos. Mater. 5 (1) (1971) 58–80.
- [68] G. Vasconcelos, P.B. Lourenço, C.A.S. Alves, J. Pamplona, Experimental characterization of the tensile behaviour of granites, Int. J. Rock Mech. Min. Sci. 45 (2) (2008) 268–277.
- [69] A.T. Vermeltfoort, D.R.W. Martens, G. Van Zijl, Brick-mortar interface effects on masonry under compression, Can. J. Civ. Eng. 34 (11) (2007) 1475–1485.
- [70] A.T. Vermeltfoort, T.M.J. Raijmakers, Shear tests on masonry walls, Tech. Rep., Technische Universiteit Eindhoven TU Delft, 1993.
- [71] J.Y. Wu, J. Li, R. Faria, An energy release rate-based plastic-damage model for concrete, Int. J. Solids Struct. 43 (3–4) (2006) 583–612.
- [72] M. Yassin, Nonlinear analysis of prestressed concrete structures under monotonic and cyclic loads, PhD thesis, University of California, Berkeley, 1994.
- [73] K. Zhou, H.-M. Chen, Y. Wang, D. Lam, A. Ajayebi, P. Hopkinson, Developing advanced techniques to reclaim existing end of service life (eosl) bricks-an assessment of reuse technical viability, Develop. Built Environ. 2 (2020) 100006.